WRC RESEARCH REPORT NO. 28

BOUNDARY EFFECTS ON JET FLOW PATTERNS RELATED TO WATER QUALITY AND POLLUTION PROBLEMS

by

W. Hall C. Maxwell
Assistant Professor of Civil Engineering
and
Hormoz Pazwash
Research Assistant in Civil Engineering

University of Illinois at Urbana-Champaign

FINAL REPORT

Project No. B-017-ILL

July 1, 1967 — December 31, 1969

The work upon which this publication is based was supported by funds provided by the U.S. Department of the Interior as authorized under the Water Resources Research Act of 1964, P.L. 88-379
Agreement No. 14-01-0001-1498

UNIVERSITY OF ILLINOIS
WATER RESOURCES CENTER
3220 Civil Engineering Building
Urbana, Illinois 61801

January 1970

ABSTRACT

BOUNDARY EFFECTS ON JET FLOW PATTERNS RELATED TO WATER QUALITY AND POLLUTION PROBLEMS

An experimental and analytical study of the modification of jet flow patterns by a nearby free surface and nearby horizontal or gently downward sloping plane bed is described. The patterns were found to be radically different from those for a deeply submerged jet. Both the free surface and bed tend to attract the jet and both cause spreading of the flow in their proximity. One boundary generally proves to be dominant, depending upon the geometrical parameters.

The analytic study used Reichardt's hypothesis and its generalization for momentum, mass and heat flux by Alexander, Baron & Comings. The techniques are first applied to predict the effect of finite nozzle size on deeply submerged jet flows. Then the effect of the free surface on a shallow submerged jet is studied. A strong influence by a small initial upward deflection of the jet is indicated. A preliminary suggestion is made for a mathematical model to represent a shallow submerged jet in a shallow reservoir.

The results may be applied in the study or design of discharge outlets, syphon spillways, hydraulic breakwaters and diffusion of tracers in streams. The diffusion of momentum, mass or heat may be studied using the analytic techniques.

Maxwell, W. Hall C., and Pazwash, Hormoz
BOUNDARY EFFECTS ON JET FLOW PATTERNS RELATED TO WATER QUALITY AND POLLUTION PROBLEMS
Completion Report to Office of Water Resources Research, Department of the Interior, Washington, D.C., January 1970, 84 pp.
KEYWORDS—*boundaries (surfaces)/ *diffusion/ flow characteristics/ *flow profiles/ fluid flow/ *free surfaces/ free turbulence/ heat flux/ hydraulics/ *jets/ mass flux/ momentum flux/ similarities/ temperature/ tracers

CONTENTS

LIST OF FIGURES

LIST OF TABLES

NOTATION

The following symbols are used in this report:

A_o = efflux area of jet

B = constant in Eq. 28

b_ψ = general jet width parameter

b = jet width parameter for momentum flux

C_ψ = general spreading coefficient; defined by Eq. 34

C = spreading coefficient for momentum flux

c_p = specific heat of fluid

D = diameter of nozzle or height of slot

exp = exponential function

erf = error function

$f(y/x)$ = function of y/x

$G(\eta)$ = function of η defined by Eq. 70

h = vertical distance below maximum flux for centerline profiles

j = exponent; $j = 0$ for plane symmetry, $j = 1$ for axial symmetry

ℓ = mixing length

ln = natural logarithm

log = logarithm to base 10

m = subscript indicating axial value, except for x_m

o = subscript indicating efflux value, except for x_o

$P(\zeta)$ = normal probability function, defined by Eq. 50

$P(\chi^2|2,\lambda)$ = non-central chi-square probability function, with two degrees of freedom and non-centrality parameter λ

$P(\chi^2|\nu)$ = chi-square probability function with ν degrees of freedom

p = fluid pressure or subscript denoting peak value

p' = fluctuation from time mean value of p.

r = radius defined by Eq. 62

s = radial polar co-ordinate in plane of nozzle discharge or rectangular co-ordinate in y direction in plane of slot discharge, or lateral rectangular co-ordinate for shallow submerged jet

$s_{\frac{1}{2}}$ = value of s for which $[\overline{u^2}/(\overline{u^2})_p]^{\frac{1}{2}} = 0.5$

S = slope of bed

t = dummy variable in Eq. 50, or time

u = instantaneous velocity in x direction

u' = fluctuation from time mean value of u

v = instantaneous velocity in y direction

v' = fluctuation from time mean value of v

w_i = concentration of i^{th} component; mass per unit fluid mass

x = co-ordinate in direction of jet axis

x_m = measured value of x

x_s = value of x at which maximum flux reaches free surface

x_o = zero correction or origin shift for x

y = co-ordinate normal to slot edge for plane symmetry; radial co-ordinate for axial symmetry

z = vertical rectangular co-ordinate

z_o = vertical submergence of nozzle centerline below free surface

z_1 = vertical distance from nozzle centerline to bed when $x_m = 0$

z_m = vertical co-ordinate of maximum flux

$\Gamma(x)$ = gamma function, argument x

ϵ = apparent kinematic viscosity

η = dimensionless vertical distance defined by Eq. 68

γ = angular polar co-ordinate associated with s for axial symmetry

ζ = argument of normal probability function, defined by Eq. 51 or Eq. 52

θ = small initial angular deflection of jet

θ_1 = temperature difference from ambient at a point in the fluid

Λ_Ψ = function of x, defined by Eq. 25 and Eq. 26

λ = non-centrality parameter for non-central chi-square probability function; defined by Eq. 45

ν = degrees of freedom for chi-square probability function; defined by Eq. 48, or kinematic viscosity of fluid

ρ = fluid density

σ_x = normal stress

τ_{xy} = shear stress

χ^2 = argument of non-central chi-square distribution; defined by Eq. 45

$\Psi = \rho w_i$ for mass flux; $= \rho c_p \theta_1$ for heat flux; $= \rho u$ for momentum flux.

I. INTRODUCTION

Many problems in water resources design are associated with submerged jet flow patterns modified by the existence of nearby rigid boundaries, free water surfaces, and density or temperature differences between the effluent and receiving water, or by the fact that the jet flow discharges into a moving stream. Such boundary conditions play an important role in such diverse problems as, for example: the prediction of recycling temperatures for cooling of thermal power plants; the design of discharge outlets; the behavior of a sediment laden stream entering a reservoir or ocean; the design of syphon spillway outlets; the use of tracers injected into penstocks in acceptance tests for turbines; and the diffusion of tracers or pollutants in streams or reservoirs. All of these problems may be to a degree idealized as jet flow patterns subjected to modifying boundary conditions.

The purpose of this investigation is to isolate and examine in detail the influence of two particular boundary conditions on submerged turbulent jet flow patterns, namely: the influence of a nearby free water surface, and the influence of a nearby horizontal or gently sloping plane bottom. The investigation is confined to those jets for which the density and temperature of the effluent and receiving water are the same. However, use is made of analytic models which may be adapted more generally.

A previous report (9)[1] presented experimental data on the modification of submerged jet flow patterns by a nearby free water

[1] Numerals in parentheses refer to corresponding items in List of References.

surface. An analytic model capable of predicting some features of such a flow quantitatively and others qualitatively is presented herein. This aspect of the investigation will be referred to as a study of shallow submerged jets in deep reservoirs.

The other objective of the present investigation was to collect experimental data on the behavior of a submerged jet subject to the influence of both a free water surface and a plane, horizontal or sloping lower fixed boundary. The data, together with some preliminary analytic analysis is presented herein and will be referred to as a study of shallow submerged jets in shallow reservoirs.

In order to provide some further information on the utility of the analytic model it is applied to the prediction of the flow pattern close to the nozzle of a deeply submerged turbulent jet.

The work upon which this report is based was supported by a matching grant using funds provided by the Office of Water Resources Research, United States Department of the Interior through the Water Resources Center, University of Illinois, and by the University of Illinois. The investigation also benefited from the National Science Foundation's continuing support of the computational facilities of the Department of Computer Science, University of Illinois.

The authors expressed their appreciation to Mr. Jay Miller, Physical Sciences Staff Assistant in the Department of Civil Engineering and to Messrs. Bruce Scott, Gary Cinnamon, Abolghassem Keramati, Ramana Murty, Malik Hussain, Armen Assaturian, Toby Frevert, and Michael Theobold, student assistants, who assisted in the development of the apparatus and in procuring data; and to Mrs. Joanne Garth who typed the manuscript.

II. LITERATURE REVIEW

II. 1. Basic Assumptions for Analytic Models

Assumptions which are common to some previously applied methods of solution for submerged turbulent jet flows may be conveniently considered together. Assuming that the flow is steady, incompressible, plane- or-axisymmetric, that there are no external forces and that the viscosity is constant throughout the flow field the Navier-Stokes equations give (12), for the axial flow direction, x:

$$u \frac{\partial u}{\partial x} + v \frac{\partial u}{\partial y} = - \frac{1}{\rho} \frac{\partial p}{\partial x} + \frac{\nu}{y^j} \frac{\partial}{\partial y} \left(y^j \frac{\partial u}{\partial y}\right) + \nu \frac{\partial^2 u}{\partial x^2} \qquad (1)$$

Herein $j = 0$ for plane-symmetry and $j = 1$ for axial symmetry; y = the cordinate normal to the axis; u = the instantaneous velocity in the x direction; v = the instantaneous velocity in the y direction; ρ = fluid density; p = pressure; and ν = kinematic viscosity of the fluid. The term at the extreme right of Eq. 1 is usually dropped on the basis of the boundary layer approximations although this is not necessary in view of a later assumption about terms containing ν. The equation of continuity is given by:

$$\frac{\partial u}{\partial x} + \frac{1}{y^j} \frac{\partial}{\partial y} \left(y^j v\right) = 0 \qquad (2)$$

Eq. 1 and Eq. 2 may be combined to give:

$$\frac{\partial u^2}{\partial x} + \frac{1}{y^j}\frac{\partial}{\partial y}\,(y^j\ uv) = -\frac{1}{\rho}\frac{\partial p}{\partial x} + \frac{\nu}{y^j}\frac{\partial}{\partial y}\left[y^j\ \left(\frac{\partial u}{\partial y} - \frac{\partial v}{\partial x}\right)\right] + 2\nu\frac{\partial^2 u}{\partial x^2} \qquad (3)$$

Applying Reynolds rules of averages (13) the time average values are then related by:

$$\frac{\partial \overline{u^2}}{\partial x} + \frac{1}{y^j}\frac{\partial}{\partial y}\,(y^j\ \overline{uv}) = -\frac{1}{\rho}\frac{\partial \bar{p}}{\partial x} + \frac{\nu}{y^j}\frac{\partial}{\partial y}\left[y^j\left(\frac{\partial \bar{u}}{\partial y} - \frac{\partial \bar{v}}{\partial x}\right)\right] + 2\nu\frac{\partial^2 \bar{u}}{\partial x^2} \qquad (4)$$

Denoting, for example, the time average value of the axial velocity by $\bar{u}$ and its fluctuation about the average by u' the following relationships for the velocity components and pressure may be written:

$$u = \bar{u} + u';\ v = \bar{v} + v';\ p = \bar{p} + p' \qquad (5)$$

Substitution of Eqs. 5 in Eq. 4 and further application of Reynolds rules of averages, assuming that the mean values are taken over a sufficiently long period of time for them to be completely independent of time, yields:

$$\bar{u}\frac{\partial \bar{u}}{\partial x} + \bar{v}\frac{\partial \bar{u}}{\partial y} = \frac{1}{\rho}\frac{\partial \sigma_x}{\partial x} + \frac{1}{\rho y^j}\frac{\partial}{\partial y}\,(y^j\ \tau_{xy}) \qquad (6)$$

in which (14)

$$\sigma_x = -\bar{p} + 2\mu\frac{\partial \bar{u}}{\partial x} - \rho\overline{u'^2} \qquad (7)$$

and

$$\tau_{xy} = \mu \left(\frac{\partial \bar{u}}{\partial y} + \frac{\partial \bar{v}}{\partial x} \right) - \rho \overline{u'v'} \tag{8}$$

with μ = dynamic viscosity of the fluid; σ_x = total normal stress; and τ_{xy} = total shear stress. The total stresses are composed of the usual laminar stresses plus apparent or Reynolds stresses resulting from the turbulent fluctuations.

Averaging the continuity equation in the same fashion yields:

$$\frac{\partial \bar{u}}{\partial x} + \frac{1}{y^j} \frac{\partial}{\partial y} \left(y^j \bar{v} \right) = 0 \tag{9}$$

Two assumptions which are generally applied to simplify the above equations for application to submerged jet flows are (a) that momentum is conserved and (b) that the Reynolds stress terms in Eq. 8 and Eq. 9 are generally much larger than the viscous terms which may be ignored. As a consequence of the first assumption the pressure gradient becomes zero and the normal stress may be considered to be changed by a constant value ($\bar{p}$). The simplified system of equations is then:

$$\bar{u} \frac{\partial \bar{u}}{\partial x} + \bar{v} \frac{\partial \bar{u}}{\partial y} = \frac{1}{\rho} \frac{\partial \sigma'_x}{\partial x} + \frac{1}{\rho \, y^j} \frac{\partial}{\partial y} \left(y^j \tau_{xy} \right) \tag{10}$$

where

$$\sigma_x' = \sigma_x - \bar{p} = - \rho \overline{u'^2} \tag{11}$$

and

$$\tau_{xy} = - \rho \overline{u'v'} \tag{12}$$

An equivalent form of the above equations is obtained by dropping the pressure gradient and viscous terms in Eq. 4 with the result that:

$$\frac{\partial \overline{u^2}}{\partial x} + \frac{1}{y^j} (y^j \overline{uv}) = 0 \tag{13}$$

Comparison of Eq. 13 with the system of Equations 10, 11, and 12 shows that the Reynolds stress terms are absorbed in the left-hand side of Eq. 13.

II. 2. Assumptions by Boussinesq, Prandtl, and Others

One class of solutions assumes that the apparent normal stress, σ_x' is negligible in comparison with the apparent shear stress so that the basic equations may be written

$$\bar{u} \frac{\partial \bar{u}}{\partial x} + \bar{v} \frac{\partial \bar{u}}{\partial y} = \frac{1}{\rho y^j} \frac{\partial}{\partial y} (y^j \tau_{xy}) \tag{14}$$

$$\tau_{xy} = - \rho \overline{u'v'} \tag{15}$$

Further simplification leading to solutions is then obtained by making suitable assumptions about the apparent shearing stress.

Boussinesq assumed that (15)

$$\tau_{xy} = \rho \, \epsilon \frac{\partial \bar{u}}{\partial y} \tag{16}$$

in which ϵ is an apparent kinematic viscosity. ϵ has the disadvantage that it is not a property of the fluid but depends on the mean velocity $\bar{u}$. It is therefore necessary to develop an empirical relationship between the apparent viscosity and the mean velocity field. Prandtl (15) proposed a relationship which is valid only for free turbulent flows, namely, that the apparent viscosity is proportional to the maximum difference in time-mean velocity multiplied by the width of the mixing zone, b, at any cross-section of the flow. In the case of submerged jets the minimum velocity may be taken to be zero so that the assumption is simplified to:

$$\epsilon \propto b \, \bar{u}_m \tag{17}$$

For a circular jet a further simplification is possible since it can be demonstrated (16) that $b \propto x$ and $\bar{u}_m \propto 1/x$ so that Eq. 17 implies that ϵ is constant. Similar reasoning for the plane-symmetric jet yields $\epsilon \propto x^{1/2}$.

Solutions have also been obtained (16) using Prandtl's mixing length hypothesis

$$\tau = \rho \ell^2 \left|\frac{\partial \bar{u}}{\partial y}\right| \frac{\partial \bar{u}}{\partial y} \tag{18}$$

or its extension

$$\tau = \rho \ell^2 \frac{\partial \bar{u}}{\partial y} \sqrt{\left(\frac{\partial \bar{u}}{\partial y}\right)^2 + \ell_1^2 \left(\frac{\partial^2 \bar{u}}{\partial y^2}\right)^2} \tag{19}$$

in which ℓ and ℓ_1 are mixing lengths.

For application of these hypotheses it is necessary to make assumptions about the mixing lengths. It is usually assumed that the mixing length, ℓ, is proportional to the width of the jet, b, and constant across any section. In addition, it is possible to use von Karman's similarity hypothesis (15)

$$\ell \propto \left| \frac{\partial \bar{u} / \partial y}{\partial^2 \bar{u} / \partial y^2} \right| \tag{20}$$

One may also make use of Taylor's vorticity transfer hypothesis (16) although this has a completely different basis from the methods discussed here.

A critical examination of some of the methods cited above is presented by Alexander et al (2).

II. 3. Reichardt's Hypothesis

Reichardt (11) used Eq. 13 to obtain solutions and his method therefore does not assume that the apparent normal stress term is negligible. He made the assumption that

$$\overline{uv} = -\frac{b}{2} \frac{db}{dx} \frac{\partial \overline{u^2}}{\partial y} \tag{21}$$

in which b is a function of x only.

Eq. 13 may then be simplified to:

$$\frac{\partial \overline{u^2}}{\partial x} - \frac{b}{2}\frac{db}{dx}\frac{1}{y^j}\frac{\partial}{\partial y}\left(y^j \frac{\partial \overline{u^2}}{\partial y}\right) = 0 \qquad (22)$$

Eq. 22 has a solution given by

$$\overline{u^2} = \frac{B}{b^{j+1}} \exp\left[-(y/b)^2\right] \qquad (23)$$

in which B = a constant which may be evaluated using the condition that momentum is conserved.

Reichardt proposed no phenomenological basis for his hypothesis. Alexander et al (2) indicate, however, that such a basis may be developed.

The retention of the apparent normal stress in Reichardt's solution avoids the necessity of neglecting $\partial \overline{u'^2}/\partial x$. Fig. 1 shows a comparison of measurements of $\sqrt{\overline{u'^2}}/u_m$ by Corrsin (3) with a curve fitted to measurements of the quantity treated as $\bar{u}/\bar{u}_m$ by Albertson et al (1) for axially symetric jets. The measurements by Albertson et al may in fact represent $\sqrt{\overline{u^2}} / \sqrt{(\overline{u^2})_m}$, in which the subscript m denotes the axial value, since the experiments were conducted using an impact tube, except for the lowest velocities. There is some question of interpretation for measurements taken with impact tubes, two interpretations being common (6). Moreover, Hinze contends that the measurments by Corrsin may be low (7). It is clear, however, that $\sqrt{\overline{u'^2}}$ is not negligibly small in comparison to $\bar{u}$ or $\sqrt{\overline{u^2}}$, particularly

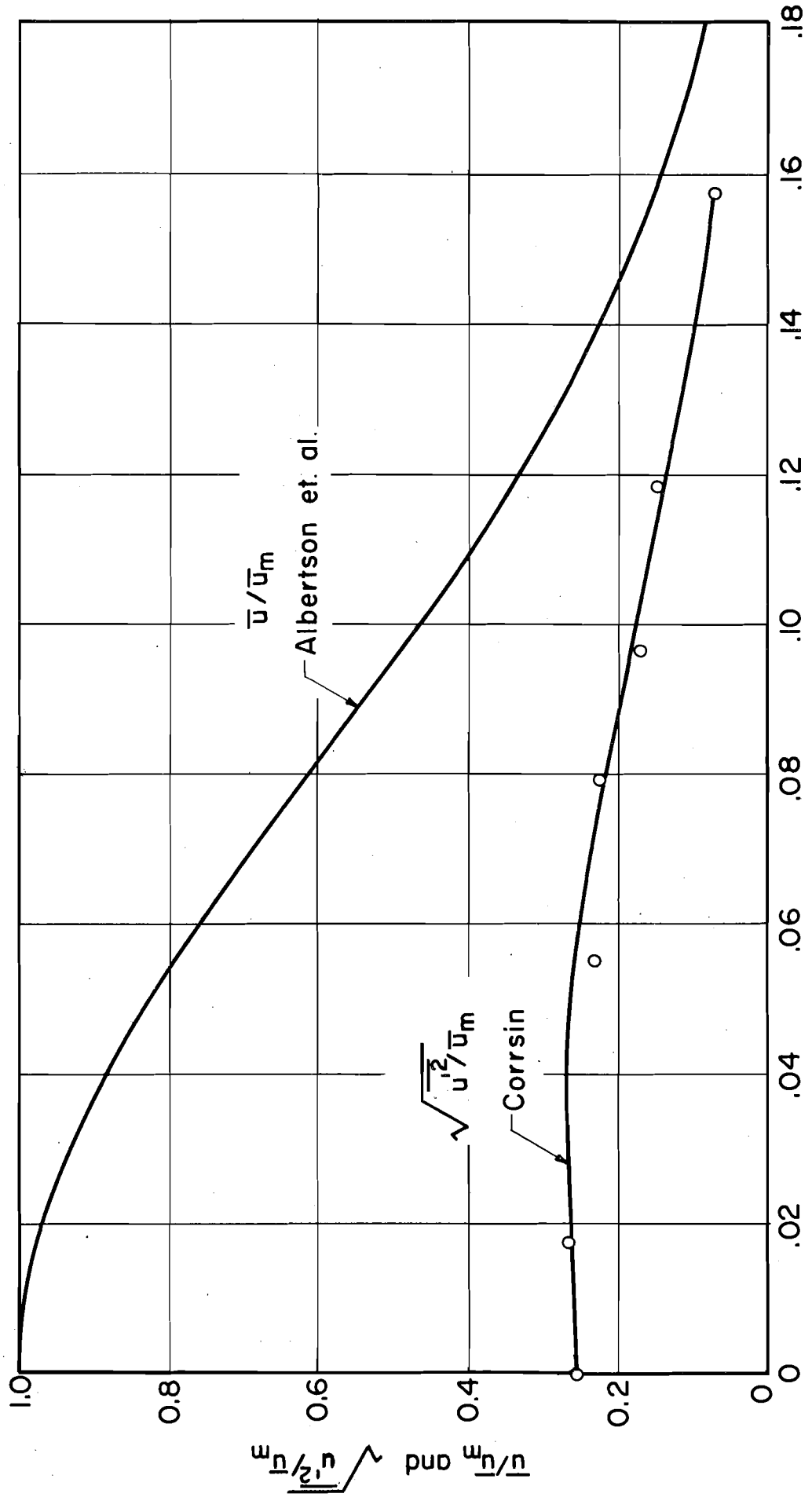

Fig. 1 — Comparison of fluctuation and mean for axial velocity component.

near the edge of the jet. It would, therefore, appear desirable to retain $\overline{u'^2}$ and its derivatives in the analysis.

Hinze (8) presents a critical examination of Reichardt's hypothesis.

II. 4. Generalization of Reichardt's Hypothesis

Alexander et al (2) proposed the use of a generalized version of Reichardt's hypothesis to obtain analytical predictions for submerged turbulent jet flows involving complicated boundary conditions.

A generalized differential equation for the flux of mass, heat, or momentum may be obtained for symmetric free turbulent jets. When it is assumed that the mean flow is steady, that pressure is uniform throughout the flow field, there are no chemical transformations, no heat release or absorption by chemical or physical process, that the amount of sensible heat formed by conversion from kinetic energy is negligible, and that molecular transport is negligible, this flux equation takes the form (2)

$$\frac{\partial \overline{\Psi u}}{\partial x} + \frac{1}{y^j} \frac{\partial}{\partial y}(y^j \overline{\Psi v}) = 0 \qquad (24)$$

Herein the bars denote averages with respect to time; for mass flux, $\Psi = \rho w_i$, in which w_i = concentration of the i^{th} component expressed as mass per unit mass of fluid; for heat flux, $\Psi = \rho c_p \theta_1$, in which c_p = specific heat of the fluid and θ_1 = temperature difference from ambient at a point in the fluid; for momentum flux, $\Psi = \rho u$.

In the specific case of momentum flux with constant density Eq. 24 becomes identical to Eq. 13.

Alexander et al (2) proposed a generalization of Reichardt's hypothesis by making the assumption that

$$\overline{\Psi v} = -\Lambda_{\Psi} \frac{\partial \overline{\Psi u}}{\partial y} \tag{25}$$

in which

$$\Lambda_{\Psi} = \frac{b_{\Psi}}{2} \frac{d\, b_{\Psi}}{dx} \tag{26}$$

and b_{Ψ} is a function of x only. With this assumption Eq. 24 becomes

$$\frac{\partial \overline{\Psi u}}{\partial x} - \frac{1}{y^j} \frac{b_{\Psi}}{2} \frac{d\, b_{\Psi}}{dx} \frac{\partial}{\partial y} \left(y^j \frac{\partial \overline{\Psi u}}{\partial y}\right) = 0 \tag{27}$$

Eq. 27 has the advantage, both mathematically and from an engineering viewpoint, of being linear in $\overline{\Psi u}$ so that superposition of elementary solutions may be employed. It provides the possibility of leading to mathematical solutions for cases of jet flow involving complicated boundary conditions.

The method of solution proposed by Alexander et al therefore offers much promise of providing solutions for the jet flow patterns being considered in this investigation as well as for the more complex flows cited in the introduction.

Some of the basic concepts will be detailed in the next section. Their utility will then be demonstrated by applying them to the prediction

of flux distributions just downstream from a submerged jet nozzle where the flow pattern is considerably influenced by the finite size of the nozzle. Alexander et al applied these concepts with success in the prediction of the momentum distributions across two parallel jets, issuing with the same velocity from orifices in the same plane perpendicular to the jet axes. Their attempt to predict the effect of finite nozzle size on the momentum distribution across a jet in the region of flow establishment met with less success. The analytical model did not match the data in the region around the jet axis.

The present work shows how a slight modification of Alexander, Baron, and Comings analysis will lead to successful predictions of the momentum flux distribution in the latter case. In addition, simplified solutions are found, which permit evaluation of the flux distribution using tables of the normal distribution and the chi-square distribution.

Although primary attention is focussed on the prediction of the distribution of momentum flux in the region of flow establishment of a finite axisymmetric turbulent jet the analysis is presented in general terms to show how it may be applied to the prediction of mass, heat, and momentum flux distributions for both axisymmetric and plane-symmetric flows.

III. BASIC CONCEPTS

III. 1. Elementary Solutions of the Flux Equation

A solution of Eq. 24 is given by

$$\overline{\Psi u} = \frac{B}{b_\Psi^{j+1}} \exp\left[-(y/b_\Psi)^2\right] \tag{28}$$

in which B = a constant which may be evaluated using the condition that the flux of Ψ is conserved. Then, integration over a section through the flow perpendicular to the axis of flow gives

$$(\overline{\Psi u})_o A_o = \int_o^\infty \overline{\Psi u}\, 2(\pi y)^j \, dy \tag{29}$$

in which $(\overline{\Psi u})_o$ = the efflux value of $\overline{\Psi u}$, assumed to be uniform over an orifice of area A_o, or a slot of area A_o per unit width. Combining Eq.28 and Eq.29 then results in

$$\frac{\overline{\Psi u}}{(\overline{\Psi u})_o} = \frac{A_o}{(\sqrt{\pi}\, b_\Psi)^{j+1}} \exp\left[-(y/b_\Psi)^2\right] \tag{30}$$

From Eq.30 it immediately follows that

$$\frac{(\overline{\Psi u})_m}{(\overline{\Psi u})_o} = \frac{A_o}{(\sqrt{\pi}\, b_\Psi)^{j+1}} \tag{31}$$

in which $(\overline{\Psi u})_m$ = the axial value of $\overline{\Psi u}$. Clearly then, if the axial distribution of $(\overline{\Psi u})_m$ is known Eq.31 provides an expression for b_Ψ. When this is substituted in Eq.30 the radial or lateral distribution of $\overline{\Psi u}$ is known. The only restriction on b_Ψ is that it be a function of x and not of y.

III. 2. Ideal Point or Line Source Jet

Sufficiently far downstream from the origin a real jet of finite size may be considered to behave as though it issued from a point or line source. For jets it has been observed that successive profiles of momentum flux density ratio are similar in this region (2),(17). Assuming that this behavior also applies to the heat and mass flux density ratios requires that

$$\frac{\overline{\Psi u}}{(\overline{\Psi u})_m} = f(\frac{y}{x}) \tag{32}$$

in which f is a function of y/x.

From Eq.30 and Eq.31

$$\frac{\overline{\Psi u}}{(\overline{\Psi u})_m} = \exp\left[-(y/b_\Psi)^2\right] \tag{33}$$

From a comparison of Eq. 32 with Eq. 33 it follows that

$$b_\Psi = C_\Psi x \tag{34}$$

in which C_Ψ is constant and is called the spread coefficient. Thus for an elemental point or line source jet of area δA_o

$$\frac{\overline{\Psi u}}{(\overline{\Psi u})_o} = \frac{\delta A_o}{(\sqrt{\pi}\, C_\Psi x)^{j+1}} \exp\left[-(\frac{y}{C_\Psi x})^2\right] \tag{35}$$

and

$$\frac{(\overline{\Psi u})_m}{(\overline{\Psi u})_o} = \frac{\delta A_o}{(\sqrt{\pi}\, C_\Psi x)^{j+1}} \tag{36}$$

For an axisymmetric point source of momentum flux Eq. 36 becomes

$$\frac{(\overline{\rho u^2})_m}{(\overline{\rho u^2})_o} = \frac{\delta A_o}{\pi C^2 x^2} = \frac{\delta A_o / D^2}{\pi C^2 (x/D)^2} \tag{37}$$

in which D = the diameter of a real jet of finite size, used as a reference in making axial distances non-dimensional. Thus, a log-log plot of the momentum flux density ratio versus x/D should yield a linear relationship when x/D is large enough for the real jet to behave as though it issued from a point source of momentum flux of area δA_o. Fig. 2 shows such a plot of the data obtained by Alexander et al. (2). The relationship is seen to be linear beyond ten diameters from the jet orifice. It may be concluded from Fig. 2 that the real jet behaves, beyond ten diameters, as though there were a point source jet located 6.5 diameters downstream from the physical jet. It should not, however, be concluded that this location corresponds with the downstream extremity of the potential core. The measurements show that the momentum flux density ratio = 1.000 when x/D = 2.11 and = 0.999 when x/D = 2.54. Thus, the potential core terminates in the region between these points. The behavior of the jet between the end of the potential core and the region of similarity beyond ten diameters will be clarified in the next section.

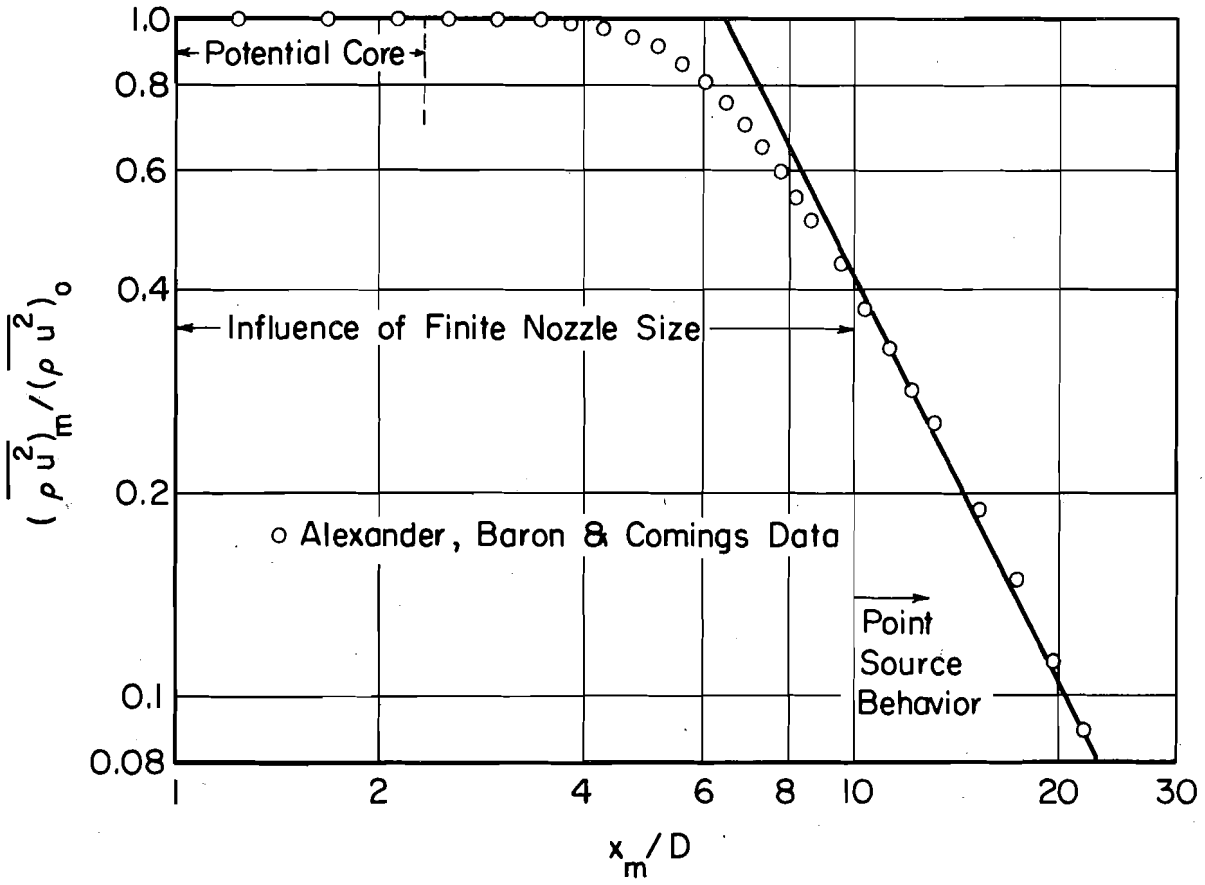

Fig. 2 — Axial variation of momentum flux density ratio using point source model.

IV. FLUX DEVELOPMENT REGION

IV. 1. Superposition of Solutions

Since linear combinations of solutions of Eq. 27 are permitted a jet of finite size may be considered to be a distribution of elemental point or line source jets of equal strength (2). The resulting distribution is

$$\frac{\overline{\Psi u}}{(\overline{\Psi u})_o} = \int_{A_o} \frac{\exp\left[-\left(\frac{y_{\delta A}}{C_\Psi x}\right)^2\right]}{(\sqrt{\pi} C_\Psi x)^{j+1}} \, dA \tag{38}$$

For axial symmetry this becomes

$$\frac{\overline{\Psi u}}{(\overline{\Psi u})_o} = \int_o^{2\pi} \int_o^{\frac{D}{2}} \frac{\exp\left[-\frac{(y^2+s^2-2ys\cos\gamma)}{C_\Psi^2 x^2}\right]}{\pi C_\Psi^2 x^2} \, sdsd\gamma \tag{39}$$

in which (s, γ) is a system of polar co-ordinates in the plane of the nozzle discharge and D = nozzle diameter.

For plane symmetry

$$\frac{\overline{\Psi u}}{(\overline{\Psi u})_o} = 2\int_o^{\frac{D}{2}} \frac{\exp\left[-\left(\frac{y-s}{C_\Psi x}\right)^2\right]}{\sqrt{\pi}\, C_\Psi x} \, ds \tag{40}$$

in which s is the rectangular co-ordinate in the plane of the slot and D = slot height.

Along the axis of symmetry y = 0 and Eq. 39 and Eq. 40 simplify to

$$\frac{(\overline{\Psi u})_m}{(\overline{\Psi u})_o} = (2)^{1-j} \left[\int_o^{2\pi} d\gamma\right]^j \int_o^{\frac{D}{2}} \frac{\exp\left[-\left(\frac{s}{C_\Psi x}\right)^2\right]}{(\sqrt{\pi}\, C_\Psi x)^{j+1}} (s)^j ds$$

$$= \operatorname{erf}\left(\frac{D}{2C_\Psi x}\right) \quad \text{for plane symmetry}$$

$$= 1 - \exp\left[-\left(\frac{D}{2C_\Psi x}\right)^2\right] \quad \text{for axial symmetry} \tag{41}$$

When x/D is very large Eq. 41 may be approximated by

$$\frac{(\overline{\Psi u})_m}{(\overline{\Psi u})_o} = \left(\frac{2}{\sqrt{\pi}}\right)^{1-j} \left(\frac{D}{2C_\Psi x}\right)^{j+1} \tag{42}$$

Eq. 42 is seen to be equivalent to Eq. 36 if the physical efflux area of the jet is replaced by δA_o. Thus, the solution given by Eq. 41 will correspond to point or line source behavior when x/D is large.

Considering once again the data for momentum flux density ratios in an axisymmetric jet plotted in Fig. 2 Eq. 41 may be written

$$\frac{x}{D} = \frac{1}{2C} \left\{-\ln\left[1 - \frac{\overline{(\rho u^2)}_m}{\overline{(\rho u^2)}_o}\right]\right\}^{-\frac{1}{2}} \tag{43}$$

Thus, a plot of x/D versus the bracketed quantity on the right hand side of Eq. 43 should be linear. Fig. 3 shows such a plot of the data, which is indeed linear beyond about 4 diameters from the nozzle. A least

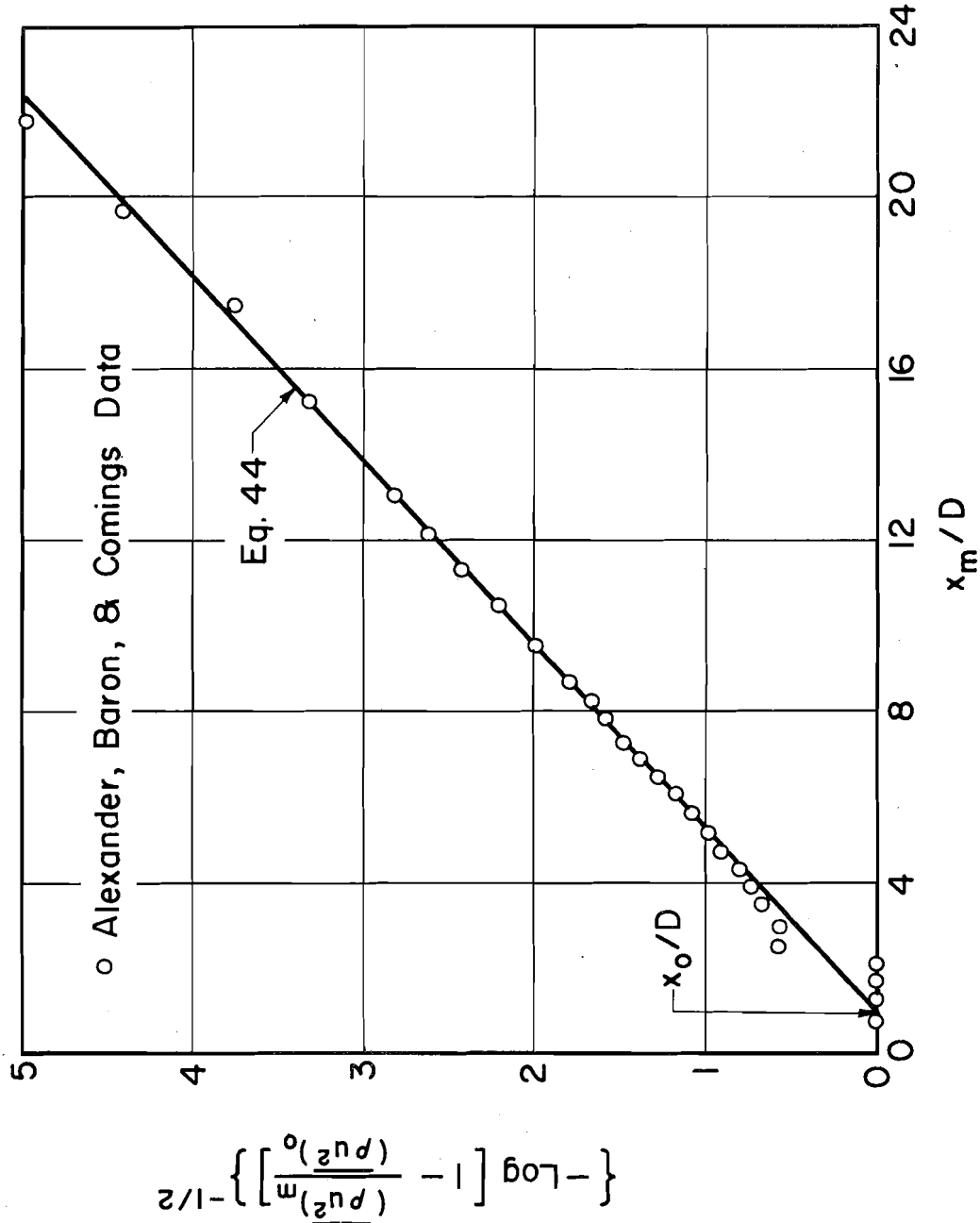

Fig. 3 — Axial variation of momentum flux density using finite nozzle model.

squares fit of the data from 2.54 diameters to 21.78 diameters yields

$$\frac{x_m}{D} = 4.264 \{- \log [1 - \frac{\overline{(\rho u^2)}_m}{(\rho u^2)_o}]\}^{\frac{1}{2}} + 0.97 \qquad (44)$$

in which x_m is used to denote the physically measured value of x. Hence, C = 0.0773, and the zero shift, $x_o/D = -0.97$. Thus, the data fit the mathematical model beyond four diameters if all the measured values of x/D are adjusted by an amount equal to x_o/D. Thus, the non-linear relationship less than ten diameters downstream from the origin in Fig. 2 is seen to result from the influence of the finite nozzle size. One would expect the zero shift, x_o/D, to be a function of the Reynold's number as was the zero shift given by the point source and line slot models utilized by Albertson et al (2). These are similar to Eq. 36 but result from a different interpretation of impact tube data (6).

IV. 2. Radial Distributions of Flux in Axisymmetric Jets

For the axially symmetric case Eq. 38 represents the integral of the circular normal distribution over an offset circle of radius D/2 and center a distance y from the point at which the flux density ratio is to be evaluated. From Ref.18, Article 26.3.24 this is the cumulative distribution function of the non-central chi-square distribution with two degrees of freedom and non-centrality parameter $2y/(C_\psi^2 x^2)$. Letting

$$\chi^2 = \frac{1}{2(C_\Psi x/D)^2} \text{ and } \frac{y}{D} = \sqrt{\frac{\lambda}{2}}\ \frac{C_\Psi x}{D} \tag{45}$$

This may be written

$$\frac{\overline{\Psi u}}{(\overline{\Psi u})_o} = P(\chi^2|\,2,\lambda) \tag{46}$$

Three different approximations to the non-central chi-square distribution function are given by Articles 26.4.27, 26.4.28 and 26.4.29 of Ref. 18. The first of these is the chi-square approximation (18)

$$\frac{\overline{\Psi u}}{(\overline{\Psi u})_o} = P(\chi^2|\,2,\lambda) \approx P\left(\frac{\nu}{2+\lambda}\,\chi^2|\,\nu\right) \tag{47}$$

in which the quantity on the right hand side is a chi-square distribution function with

$$\nu = \frac{(2+\lambda)^2}{2(1+\lambda)} \tag{48}$$

The chi-square probability function is defined by

$$P(\chi^2|\,\nu) = \left[2^{\nu/2}\,\Gamma\left(\frac{\nu}{2}\right)\right]^{-1} \int_o^{\chi^2} t^{\frac{\nu}{2}-1}\ \exp\left[-\frac{t}{2}\right]\ dt$$

and is tabulated (10), (18) for integer value of ν (degrees of freedom). From Eq. 48 there is a corresponding value of λ for each integer value

of ν, given by the positive root of the quadratic relationship. Using Eq. 45 this permits the evaluation of y/D for any selected value of $C_\Psi x/D$. C_Ψ is evaluated from a plot of the axial measurements as shown in Fig. 3 for momentum flux. Thus, using Eq. 45, 47, 48, and tables of the chi-square distribution the flux distribution may be easily evaluated.

The chi-square approximation is useful when $C_\Psi x/D$ is small. When it is large the restriction to integer degrees of freedom provides too few points to properly define the flux distribution. Table I shows the values of $\nu/(2+\lambda)$ and $\sqrt{\lambda/2}$ corresponding to integer values of ν. Use of Table I and tables of the chi-square distribution permits very rapid evaluation of the flux profiles.

The other approximations are normal approximations

$$\frac{\overline{\Psi u}}{(\overline{\Psi u})_o} = P(\chi^2 | 2,\lambda) \approx P(\zeta) \tag{49}$$

The normal probability function is defined by

$$P(x) = \frac{1}{\sqrt{2\pi}} \int_{-\infty}^{x} \exp\left[-t^2/2\right] dt \tag{50}$$

In the first normal approximation (18)

$$\zeta = \left[\left(\frac{\chi^2}{2+\lambda}\right)^{1/3} - 1 + \frac{2}{9\nu}\right] \Big/ \sqrt{\frac{2}{9\nu}} \tag{51}$$

In the second normal approximation (18)

TABLE I — CHI-SQUARE APPROXIMATION PARAMETERS

ν (1)	$\frac{\nu}{2+\lambda}$ (2)	$\sqrt{\frac{\lambda}{2}}$ (3)	ν (1)	$\frac{\nu}{2+\lambda}$ (2)	$\sqrt{\frac{\lambda}{2}}$ (3)
2	1.000	0	20	0.513	4.300
3	0.634	1.169	21	0.513	4.414
4	0.586	1.554	22	0.512	4.526
5	0.564	1.854	23	0.511	4.636
6	0.551	2.109	24	0.511	4.742
7	0.542	2.336	25	0.510	4.847
8	0.536	2.542	26	0.510	4.949
9	0.531	2.733	27	0.510	5.049
10	0.528	2.911	28	0.509	5.147
11	0.525	3.078	29	0.509	5.243
12	0.523	3.237	30	0.509	5.338
13	0.521	3.388	40	0.506	6.204
14	0.519	3.533	50	0.505	6.964
15	0.518	3.672	60	0.504	7.648
16	0.517	3.806	70	0.504	8.276
17	0.516	3.935	80	0.503	8.860
18	0.515	4.060	90	0.503	9.407
19	0.514	4.182	100	0.503	9.925

$$\zeta = \left[\frac{2\nu\chi^2}{2+\lambda}\right]^{\frac{1}{2}} - \left[2\nu-1\right]^{\frac{1}{2}} \qquad (52)$$

Neither of the normal approximations is restricted to integer values of ν.

After correcting all measured values of x/D greater than 4 by the zero shift x_o/D, as shown in Table II, the three approximations have been compared with the data of Alexander et al (2) for momentum flux distributions in an axisymmetric jet. The comparison for $x_m/D = 6$ (corresponding to x/D = 5.03) is shown in Fig. 4. It was found that, for $Cx/D > 0.39$ the first normal approximation gives a better fit near the crest of the distribution than does the second normal distribution. The second normal distribution gives a better fit near the tail than the first normal distribution. For values of $Cx/D < 0.234$ the chi-square approximation, which is simpler to compute, provides enough points to define the distribution and is not significantly different from either of the normal approximations.

Fig. 5 shows a mapping of the intersections of the two normal approximations, with the zones of best fit for each approximation indicated. From the figure, when Cx/D = 0.6 the distribution of flux may best be represented by the first normal approximation for $0 < y/D < 0.525$, and by the second normal approximation for $y/D > 0.525$.

For values of $x_m/D < 4$, Eq. 44 does not apply. It was found however, that using the value of C given by Eq. 44, namely 0.0773, and using no zero correction, leads to a good fit of the data by all three approximations. Fig. 6 shows the comparison between the data and the chi-square approximation for x/D = 1; Fig. 7 shows the comparison for x/D = 2.

TABLE II — PARAMETERS FOR AXISYMMETRIC JET DATA

$C = 0.0773$ $x_o/D = 0.97$

x_m/D (1)	x/D (2)	Cx/D (3)	Cx_m/D (4)
1	—	—	0.0773
2	—	—	0.155
4	3.03	0.234	—
6	5.03	0.389	—
8	7.03	0.543	—
10	9.03	0.698	—

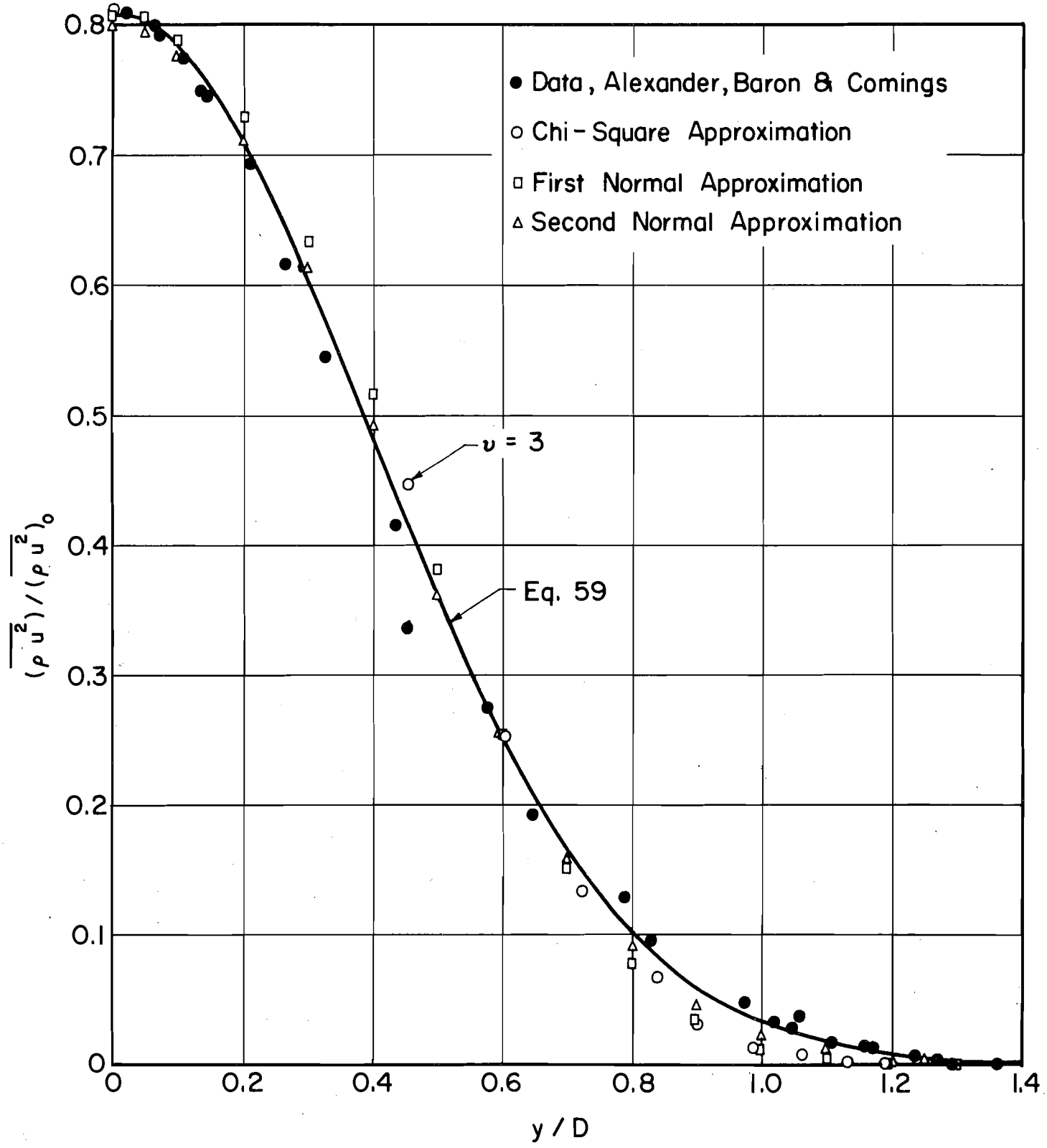

Fig. 4 — Chi-square and first and second normal approximations to radial distribution of momentum flux density ratio for $x_m/D = 6$.

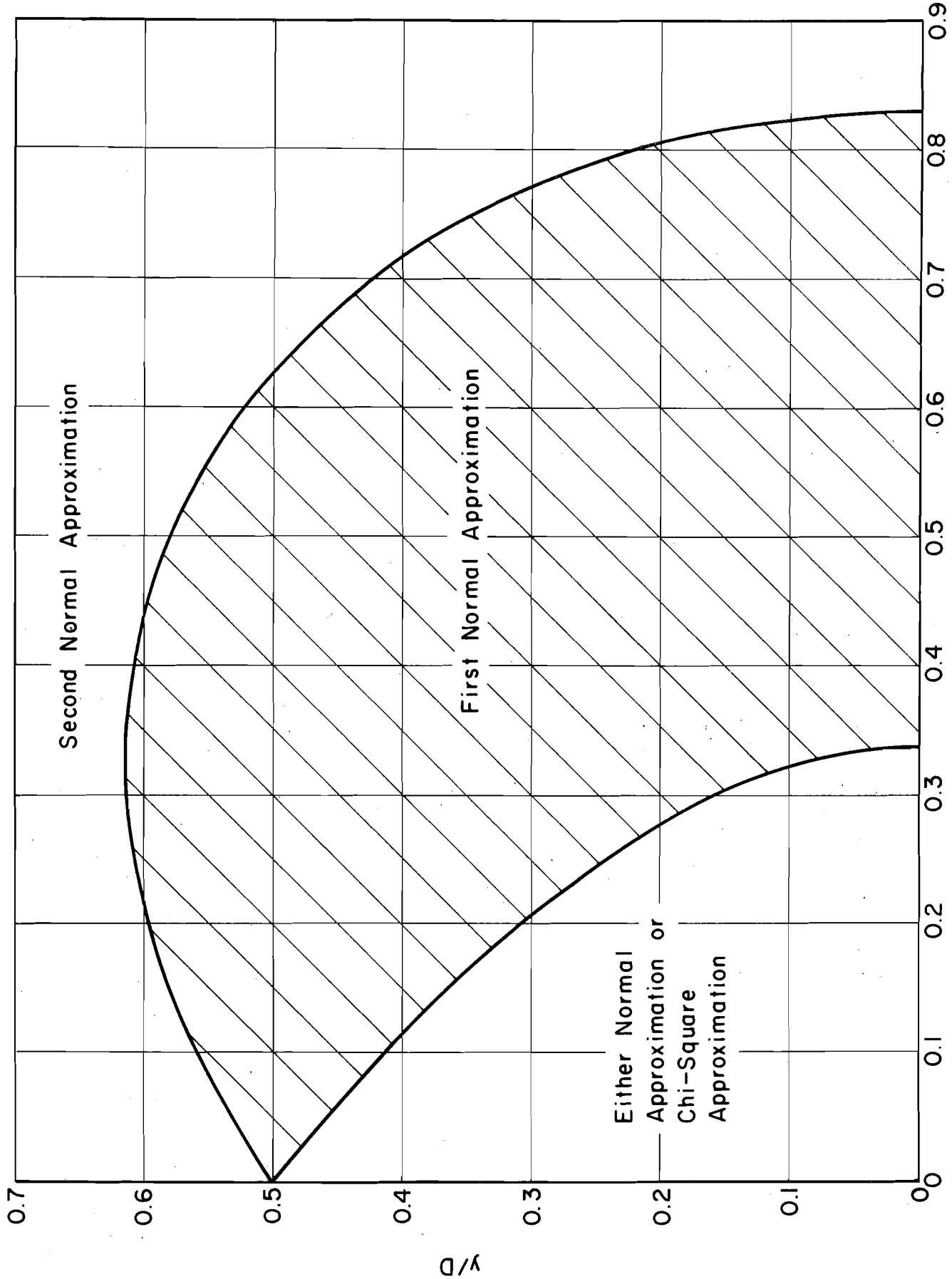

Fig. 5 — Intersections of first and second normal approximations.

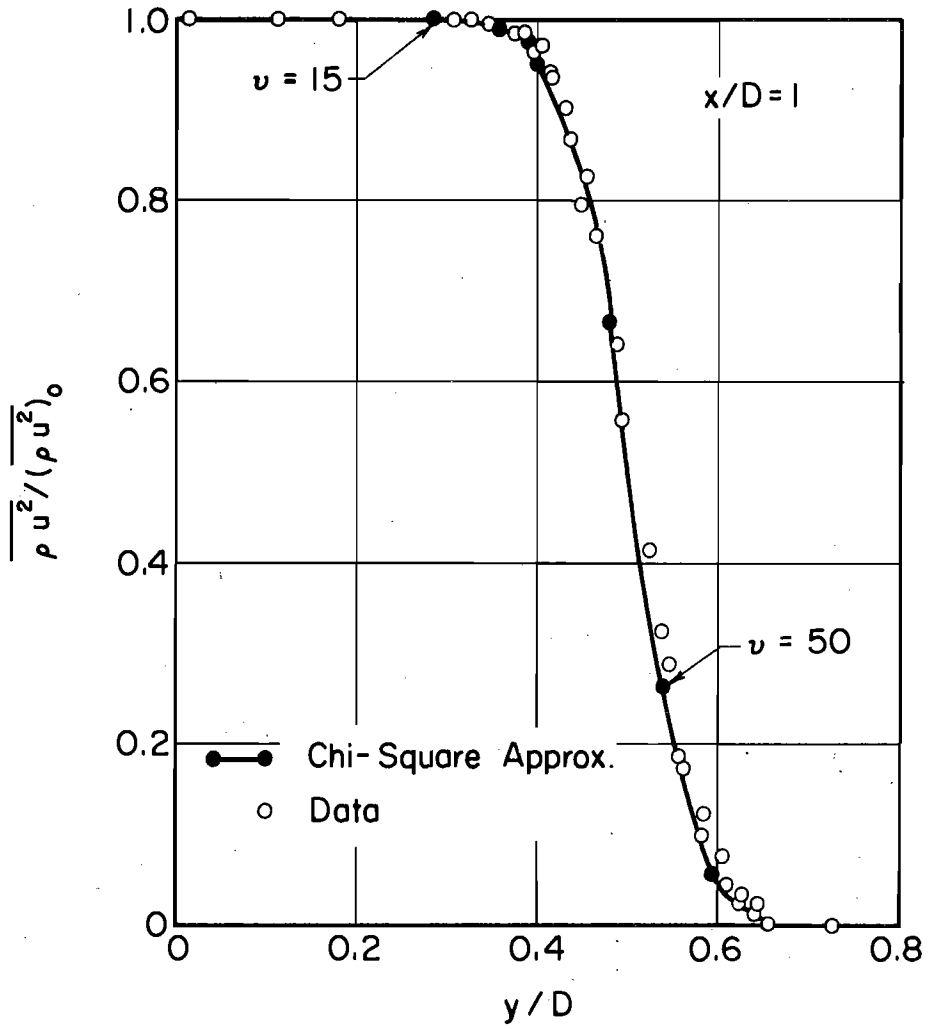

Fig. 6 — Chi-square approximation to radial distribution of momentum flux density ratio for x/D = 1.

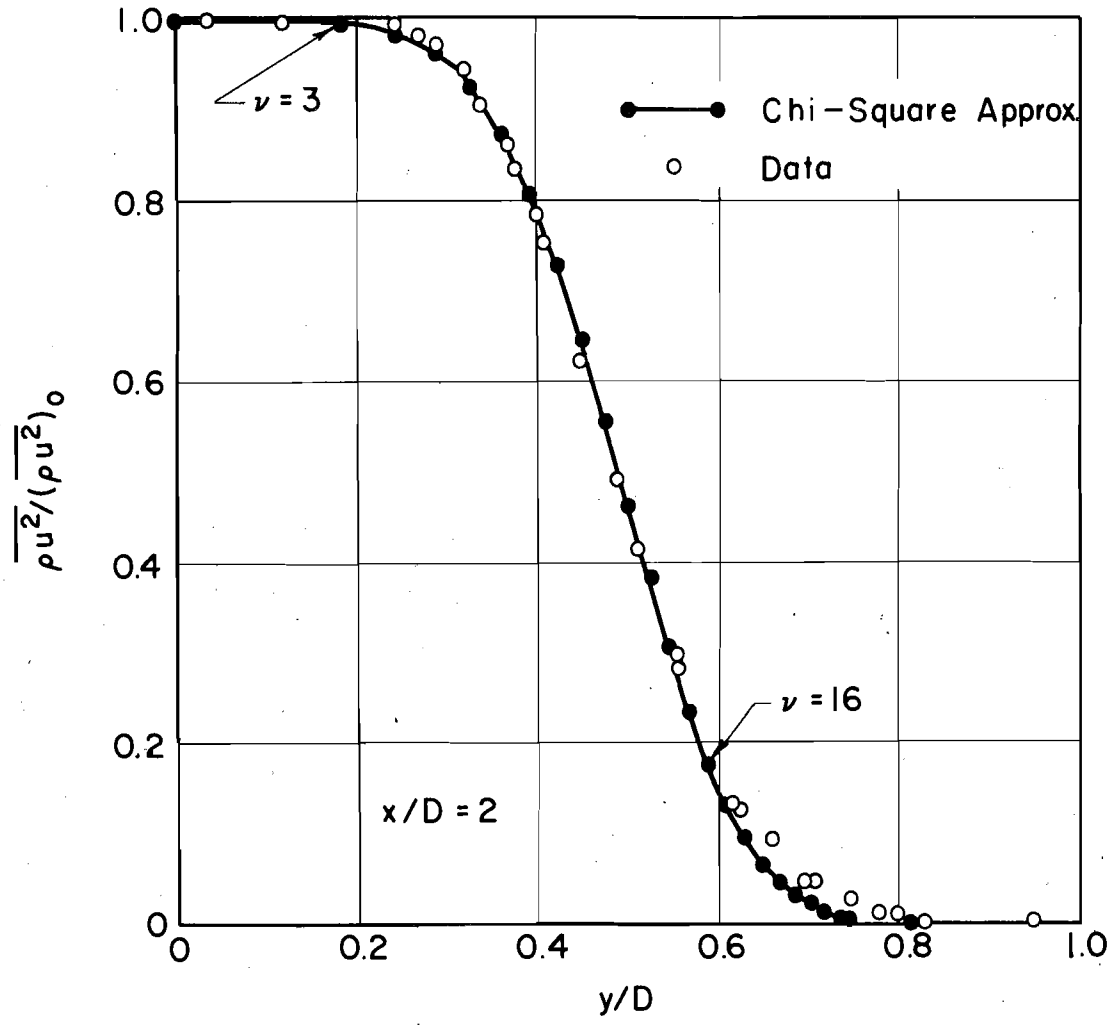

Fig. 7 — Chi-square approximation to radial distribution of momentum flux density ratio for x/D = 2.

IV. 3. Simplified Solutions Beyond Potential Core

For axisymmetric flux of momentum Eq. 31 gives

$$\frac{\overline{(\rho u^2)}_m}{\overline{(\rho u^2)}_o} = \frac{A_o}{\pi b^2} = \frac{D^2}{4b^2} \tag{53}$$

and Eq. 41 gives

$$\frac{\overline{(\rho u^2)}_m}{\overline{(\rho u^2)}_o} = 1 - \exp\left[-\left(\frac{D}{2Cx}\right)^2\right] \tag{54}$$

which is applicable for $x_m/D > 4$ (see Fig. 3). Equating Eq. 53 and Eq. 54 then yields

$$\frac{y^2}{b^2} = 4\frac{y^2}{D^2}\left[1 - \exp\left[-\left(\frac{D}{2Cx}\right)^2\right]\right] \quad \text{for } x_m/D > 4 \tag{55}$$

From Eq. 30

$$\frac{\overline{\rho u^2}}{\overline{(\rho u^2)}_m} = \exp\left[-\left(\frac{y}{b}\right)^2\right] \tag{56}$$

The combination of Eq. 55 and Eq. 56 then yields the axial distribution of momentum flux for $x_m/D > 4$

$$\frac{\overline{\rho u^2}}{\overline{(\rho u^2)}_m} = \exp\left[-4\frac{y^2}{D^2}\left\{1 - \exp\left[-\left(\frac{D}{2Cx}\right)^2\right]\right\}\right] \tag{57}$$

The solution given by Eq. 57 is compared with the data of Alexander et al (2) in Fig. 8 for $x_m/D = 4$, 6, 8, and 10, and shows good agreement with

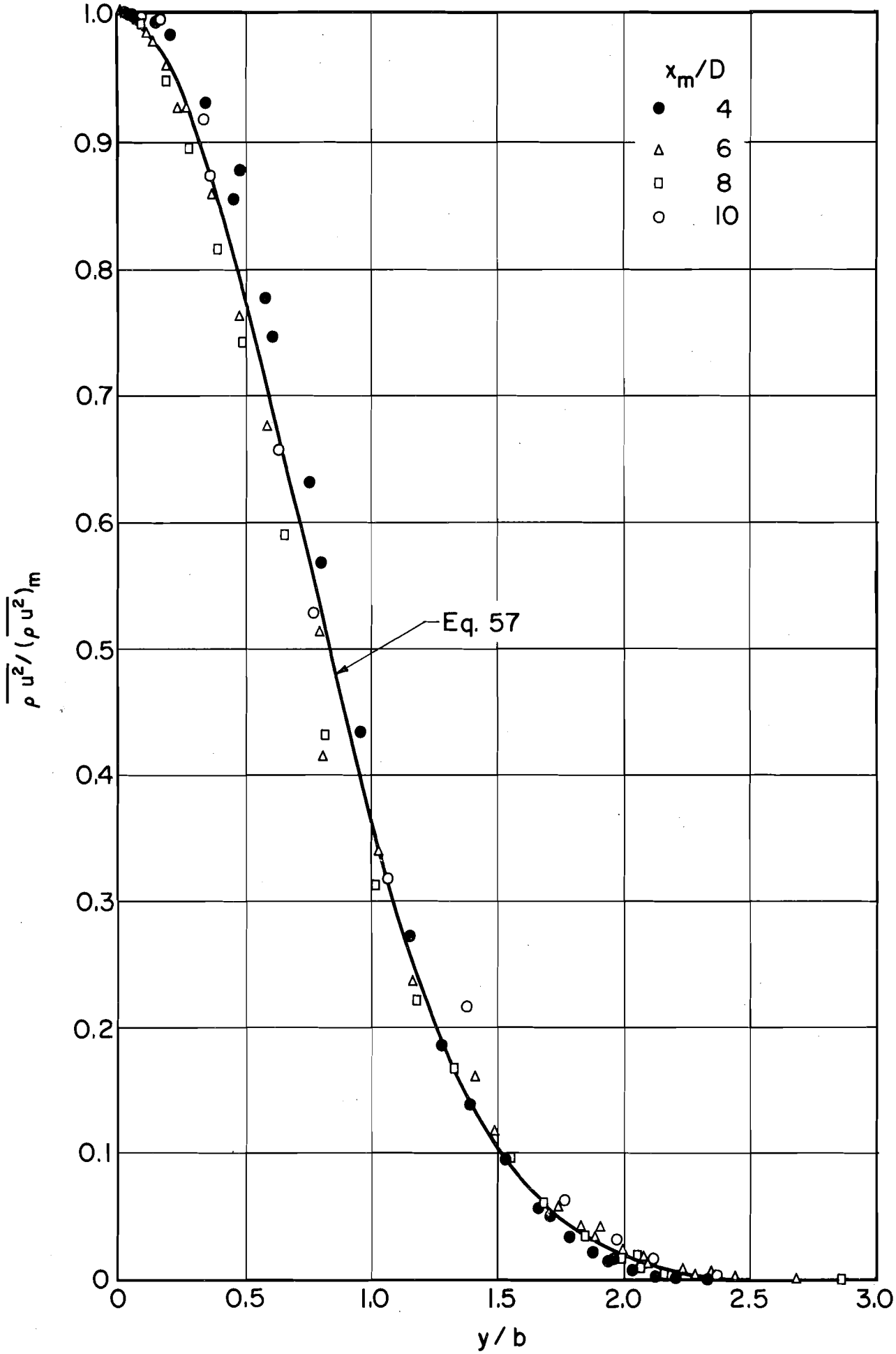

Fig. 8 — Momentum flux density ratio distribution at 4, 6, 8, and 10 diameters downstream from nozzle.

the data. Combining Eq. 54 and Eq. 57 gives

$$\frac{\overline{\rho u^2}}{\overline{(\rho u^2)}_o} = \left[1 - \exp\left[-\left(\frac{D}{2Cx}\right)^2\right]\right] \exp\left[-4\frac{y^2}{D^2}\left\{1 - \exp\left[-\left(\frac{D}{2Cx}\right)^2\right]\right\}\right] \tag{58}$$

For $x_m/D = 6$ this reduces to

$$\frac{\overline{\rho u^2}}{\overline{(\rho u^2)}_o} = 0.809 \exp\left[-3.234\frac{y^2}{D^2}\right] \tag{59}$$

Eq. 59 is plotted on Fig. 4 for comparison with the chi-square and normal approximations.

IV. 4. Summary and Discussion

Linear superposition of solutions of the generalized flux equation for axially symmetric and plane symmetric jets may be used to predict the distribution of axial flux beyond the potential core in jets of finite size. From this distribution a spread coefficient and a zero correction may be obtained. Using these, the lateral flux distributions in the region of flow establishment may be predicted.

It has been shown that, for an axially symmetric jet flow, the radial distribution of momentum flux may be obtained in the region of flow establishment using three approximations to the non-central chi-square distribution. These are the chi-square and first and second normal approximations. Moreover, beyond the potential core the distribution of axial momentum flux leads directly to a solution for the

radial distribution of momentum flux as given by Eq. 57 and Eq. 58.

The analytical model proposed by Alexander, Baron, and Comings (2) therefore shows much promise for the solution of jet flows involving complicated boundary conditions provided proper attention is given to the correction of axial distances using the zero correction derived from the axial flux distribution.

Since one of the primary objectives of the present investigation was to collect and analyze data on momentum flux distributions for shallow submerged circular jets in both shallow and deep reservoirs, the analysis in the following sections will consider only initially axisymmetric sources of momentum flux and modification of the flux patterns by the flow boundaries. This entails only application of Reichardt's original hypothesis. It is clear, however, that application of Alexander, Baron, and Comings generalized hypothesis would permit extension of the analysis to include both heat and mass flux.

V. SHALLOW SUBMERGED JETS IN DEEP RESERVOIRS

V. 1. Introduction

A previous report (9) presented a preliminary analysis of data for flow patterns downstream of a submerged circular jet nozzle directed almost horizontally and at very shallow submergence below the free surface of a reservoir. The reservoir bottom was sufficiently far below the nozzle to have negligible influence on the flow patterns.

The present investigation includes a more detailed analysis of the data. The original measurements were taken with a pitot tube aligned in the axial direction and the measurements were presumed to yield $\bar{u}$. In the present analysis the interpretation is changed and the measurements are presumed to yield $\sqrt{\overline{u^2}}$, when the density is constant. It was noted earlier that both interpretations are common (6): the present interpretation is compatible with Reichardt's hypothesis. The reader may prefer to interpret these identically, thus assuming that $\overline{u'^2}$ is negligible.

The present analysis revealed that the jet did not enter the reservoir exactly horizontally as had been supposed in the preliminary analysis. An initial upward deflection of the jet was particularly evident for data collected using a $\frac{1}{2}$-in. dia. nozzle. Close examination of the original nozzle revealed that the axis of the internal bore and the axis of the nozzle exterior were not coincident. Moreover, the nozzle was attached to the supply pipe by a threaded connection, which allows for the possiblity of misalignment, since the nozzle was set "horizontal"

by levelling the top of the pipe leading to the nozzle. The still water surface was used as a reference. Fortunately, the misalignment was such that there was negligible lateral deflection of the nozzle axis.

The possibility existed, however, that the initial upward deflection of the efflux from the nozzle was due to a density difference resulting from transfer of heat to the effluent in its passage through the pump. Consequently a series of temperature measurements was taken, with the temperature being measured at the pump suction and 6 to 8-in. directly downstream from the nozzle at intervals of three minutes. The data are presented in Table III. It is seen that there was no measurable temperature difference across the pump.

The misalignment of the nozzle axis was perhaps fortunate since it revealed that the flux pattern is extremely sensitive to small vertical deflections of the nozzle axis. Determination of the deflection angle and its effect will be dealt with in detail in a later section.

V. 2. Direction Meter Measurements

Considerable effort was expended in constructing a direction meter built-up using 2 hypodermic needles aligned in a vertical plane and 2 aligned orthogonal to them. The needles were parallel and terminated at the measurement point with 15^{o} chamfers. A support mechanism was designed to permit vertical rotation and horizontal rotation of the assembly without changing the spacial location of the end point. When aligned in the direction of the velocity vector the differential across a pair of needles was zero.

TABLE III — TEMPERATURE DATA FOR $\frac{1}{2}$-IN. NOZZLE; EFFLUX VELOCITY = 40.6 FT/SEC., SUBMERGENCE = 10 DIA.

Time in minutes (1)	Temperature at pump suction in degrees Centigrade (2)	Temperature at 6 in. $< x <$ 8 in., $y = 0$, $z = 0$ in degrees Centigrade (3)
0	19.7	19.7
3	19.7	19.7
6	19.8	19.8
9	19.8	19.8
12	19.8	19.8
15	19.8	19.8
18	19.8	19.8
21	19.8	19.8
24	19.8	19.8
Smallest division on thermometer = 0.2 C^{o}		

Measurements of direction of the velocity vectors were taken at distances of 2-ft. and 4-ft. downstream from a $\frac{1}{2}$-in. nozzle, submerged 10 dia. and discharging fluid horizontally into the reservoir with an efflux velocity of 40.6 ft/sec. Vertical angles could be read to 10 mins. and horizontal angles to 5 mins. However, the measured values could only be reproduced within 30 mins. in each direction.

The results of the measurements proved inconclusive in that it was impossible to obtain sufficient manometer deflection to detect an angle except in regions of high velocity. The data gave only a general indication that the velocity vectors corresponding to isolines for $\sqrt{\overline{u^2}} / (\sqrt{\overline{u^2}})_m$, i.e. isoflux lines, greater than 0.6 had a total angular deflection of the velocity vector from the axial direction of less than 8^o at a distance of 2-ft. downstream from the nozzle. Four feet from the nozzle the vectors corresponding to isoflux lines greater than 0.6 have a total angle of deflection less than 6^o.

The pitot tubes used for data collection were round nosed and are therefore insensitive to yaw up to 17^o inclination (19, 20). Hence, they actually respond to the magnitude of the velocity vector rather than its longitudinal component for deflection angles under 17^o. In view of the fact that angular determinations could not be made across the entire flow field it is not possible to define the error levels introduced by this effect in procuring the isoflux patterns shown in Figs. 4, 5, 6, 7 and 8 of Ref. (9).

V. 3. Mathematical Model for Jet with Small Upward Deflection

Fig. 9 provides a schematic representation of the mathematical model. The vertical co-ordinates are now represented by z and the lateral co-ordinates by s in a rectangular system to avoid confusion with the previous definition of y.

For momentum flux with constant density Eq. 27 becomes identical to Eq. 22 and is linear in $\overline{u^2}$. For a point source of momentum flux the distribution of momentum flux is then given by Eq. 33 and Eq. 34 as

$$\frac{\overline{u^2}}{(\overline{u^2})_m} = \exp\left[-\left(\frac{y}{Cx}\right)^2\right] \tag{60}$$

in which C = the spread coefficient for momentum flux.

For a jet with a small initial upward deflection the mathematics may be considerably simplified by making the approximation illustrated in Fig. 9, namely that the distribution of momentum flux downstream from an inclined point source is given by:

$$\frac{\overline{u^2}}{(\overline{u^2})_m} = \exp\left[-\left(\frac{r}{Cx}\right)^2\right] \tag{61}$$

in which

$$r^2 = s^2 + (z_o - z - \theta x)^2 \tag{62}$$

and θ = initial deflection of the jet axis.

This approximate model cannot be expected to apply for $x > z_o/\theta$, except for $\theta = 0$.

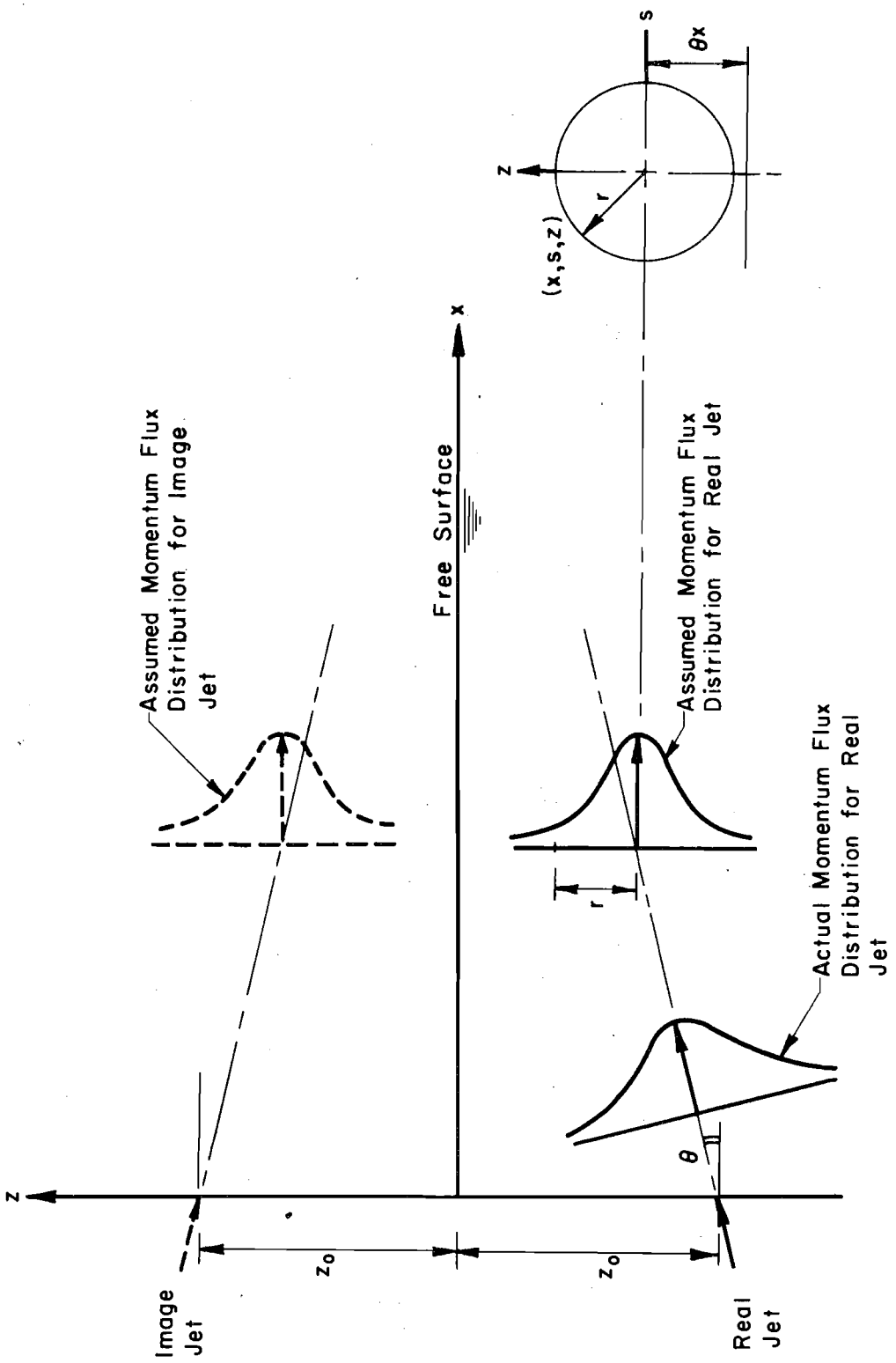

Fig. 9 — Schematic representation of mathematical model for jet with small initial upward deflection near a free surface.

Since there can be no flux of momentum across the free surface an image jet is placed equidistant above the free surface to cancel the lateral flux when z = 0. The momentum flux distribution for the real and image jet combination is then given by:

$$\frac{\overline{u^2}}{(\overline{u^2})_o} = \frac{D^2}{4C^2x^2}\left\{\exp\left[-\frac{s^2 + (z_o - z - \theta x)^2}{C^2x^2}\right] + \exp\left[-\frac{s^2 + (z_o + z - \theta x)^2}{C^2x^2}\right]\right\} \tag{64}$$

After some manipulation this may be written as

$$\frac{\overline{u^2}}{(\overline{u^2})_o} = \frac{D^2}{2C^2x^2} \exp\left[-\left(\frac{s}{Cx}\right)^2\right] \exp\left[-\left(\frac{z_o - \theta x}{Cx}\right)^2\right] F(z) \tag{65}$$

in which

$$F(z) = \exp\left[-\left(\frac{z}{Cx}\right)^2\right] \cosh\left[\frac{2z(z_o - \theta x)}{C^2x^2}\right] \tag{66}$$

The location of the maximum flux may be obtained by setting s = 0 in Eq. 65 and maximizing $\overline{u^2}/(\overline{u^2})_o$ with respect to z. This yields

$$\eta = \tanh\left[2\eta\left(\frac{z_o - \theta x}{Cx}\right)^2\right] \tag{67}$$

in which

$$\eta = \frac{z_m}{z_o - \theta x} \tag{68}$$

and z_m is the vertical co-ordinate of the maximum flux.

After some manipulation substitution of Eq. 67 in Eq. 65 yields

$$\frac{\overline{(u^2)}_m}{\overline{(u^2)}_o} = \frac{D^2}{2C^2x^2}\, G(\eta) \tag{69}$$

in which

$$G(\eta) = \frac{(1-\eta)^{\frac{(1-\eta)^2}{4\eta}}}{(1+\eta)^{\frac{(1+\eta)^2}{4\eta}}} \tag{70}$$

Eq. 67 defines the location of the filament of maximum flux. Eq. 69 describes the decay of the maximum flux in the axial direction. The momentum flux distribution is given by Eq. 65. Solutions for an initially horizontal jet may be obtained by setting $\theta = 0$.

As noted in the previous chapter Reichardt's hypothesis may be used to obtain good correlation with the data at small distances from the nozzle provided adequate attention is paid to determining the zero correction for x. Since for the present data C and θ must be determined from the experimental data at small values of x, three experimental coefficients are required, namely, x_o, θ and C. Normally θ would be prescribed. Unfortunately the apparatus had been disassembled before it was recognized that the jet had a small upward deflection, thus requiring that the determination be made from the data.

V. 4. Vertical Center-line Flux Distributions Below the Maximum

The solutions given by Eq. 64 reveal that the contribution of the second exponential term representing the image jet is very small below

the point of maximum flux when s = 0 and x is small. Thus, the lower part of the profiles may be assumed to behave as though the image jet did not exist for s = 0 and small x.

Letting the vertical distance below the point of maximum flux = h, the flux distribution in the lower region may be approximated by:

$$\frac{\overline{u^2}}{(\overline{u^2})_m} = \exp\left[-\left(\frac{h}{Cx}\right)^2\right] \tag{71}$$

Then letting $x = x_m + x_o$

$$-\ln\left[\frac{\overline{u^2}}{(\overline{u^2})_m}\right]^{\frac{1}{2}} = \frac{1}{2C^2}\left(\frac{h}{x_m+x_o}\right)^2 \tag{72}$$

The quantity on the left hand side of Eq. 72 was plotted versus $[h/(x_m + x_o)]^2$ for x_m = 1, 2 and 3 ft. using the data upon which the iso-flux patterns shown in Ref. (9) are based. The plot is shown on Fig. 10 with $x_o/D = 2$, together with Eq. 72 when C = 0.083.

V. 5. Location of Filament of Maximum Flux

When C, x_o and θ are specified Eq. 67 and Eq. 68 give the location of the filament of maximum flux letting

$$f(\eta) = \left(\frac{2}{\eta \operatorname{arctanh} \eta}\right)^{\frac{1}{2}} \tag{73}$$

manipulation of Eq. 67 and Eq. 68 yields:

$$\frac{z_m}{z_o} = \frac{\eta}{1 + \frac{\theta}{C}\eta f(\eta)} \tag{74}$$

and

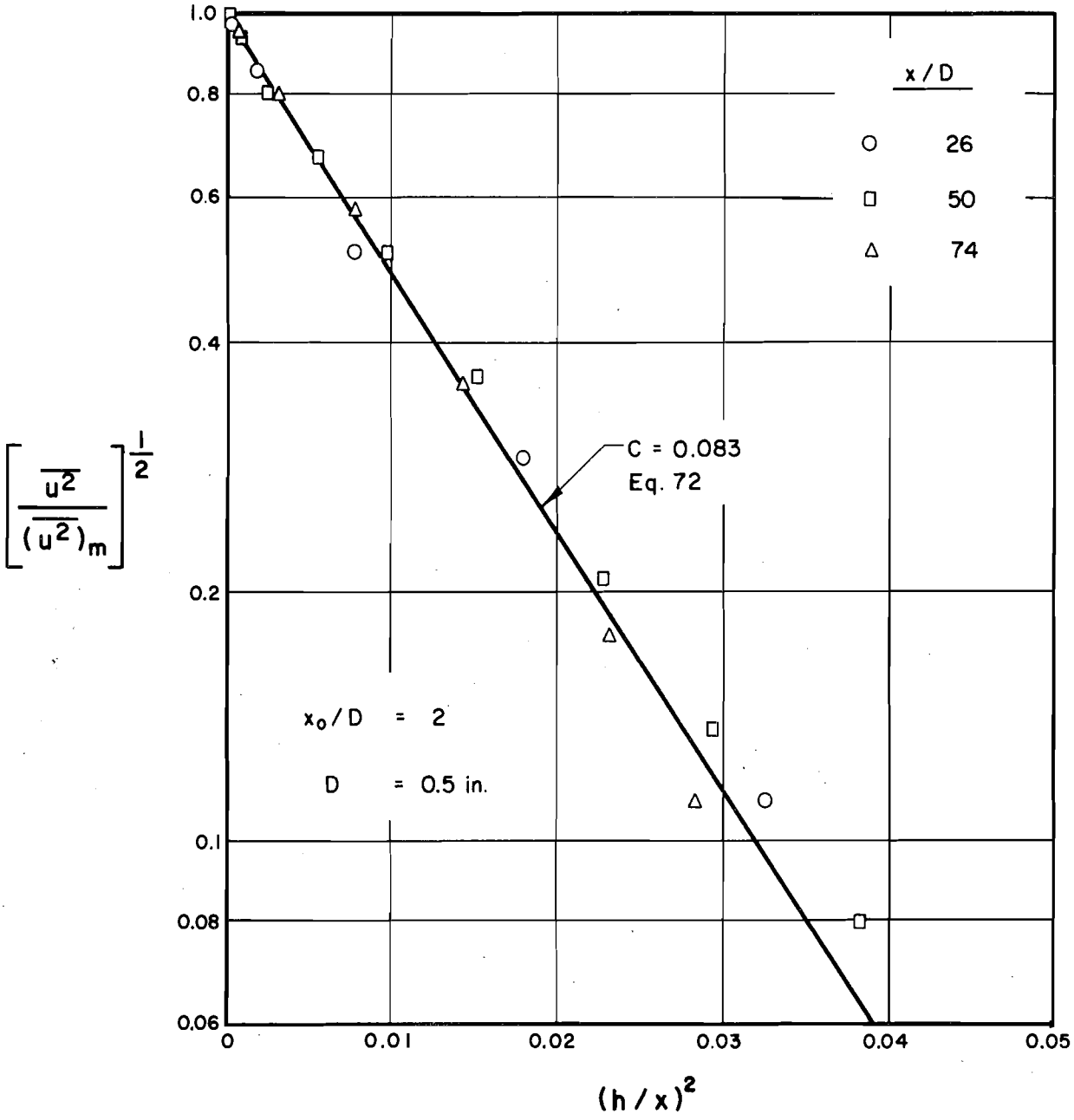

Fig. 10 — Flux distribution below the maximum at small x for a shallow submerged jet.

$$\frac{x}{z_o} = \frac{1}{C}\frac{z_m}{z_o} f(\eta) \tag{75}$$

Since η lies between 0 and 1 selection of various values of η between these limits will permit the computation of the locus of the filament of maximum flux using Eq. 73, Eq. 74 and Eq. 75. Fig. 11 shows a plot for x/z_o versus z_m/z_o for values of θ = 0, 1, 2, $2\frac{1}{2}$ and 3 degrees when C = 0.083. Also plotted are the experimental data points for the $1\frac{1}{2}$-in. diameter jet with an initial upward deflection from Ref. (9), using $x_o/D = 2$. The data are for traces of the maximum flux at three different submergences as well as from the isoflux patterns.

It was noted in Ref. (9) that there is considerable difficulty in determining the precise vertical location of the maximum flux experimentally because the vertical center-line profiles are generally flat in the region of the maximum except for small x. The determination for the isoflux patterns was more accurate than for the other data since complete profiles were taken. However, for $x/z_o = 9.8$ the profile was so flat that the maximum could be taken to lie anywhere between $z_m/z_o = 0$ and 0.36. This is indicated on Fig. 11. The data for the smaller x/z_o values, however, show close agreement with the theoretical curve for θ = 3 degrees. For x/z_o less than 6 the right hand side of Eq. 67 is approximately equal to 1, thus $\eta = 1$. From Eq. 68 then, for small x

$$1 - \theta \frac{x}{z_o} \doteq \frac{z_m}{z_o} \tag{76}$$

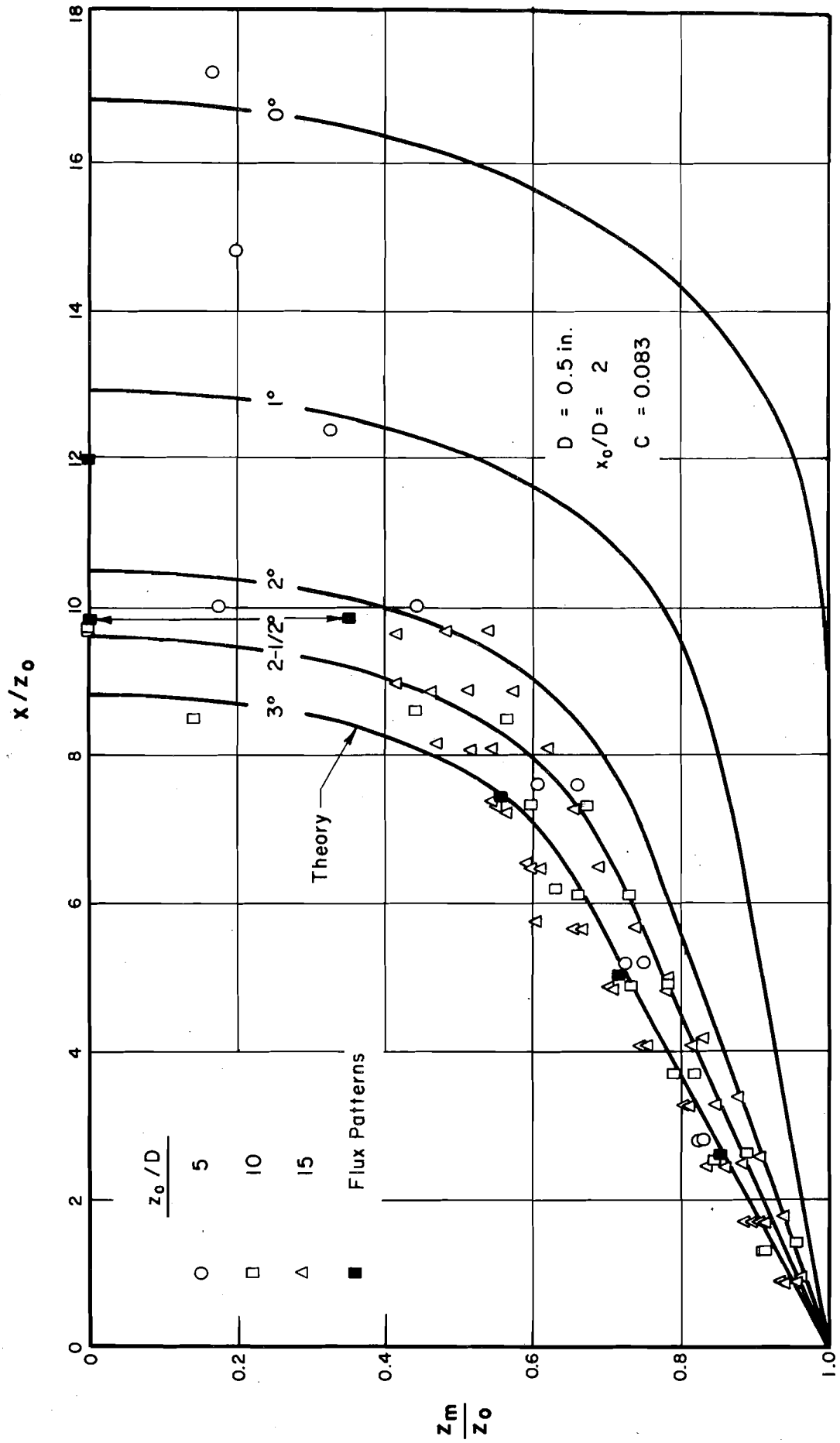

Fig. 11 — Vertical centerline location of filament of maximum flux for shallow submerged jet with small initial upward deflection.

Eq. 67 may also be used to compute the location, x_s, at which the filament of maximum flux reaches the free surface. As this occurs η becomes very small and the hyperbolic tangent term becomes approximately equal to its argument. Eq. 67 may then be simplified to

$$\frac{x_s}{z_o} = \frac{\sqrt{2}}{C + \sqrt{2}\ \theta} \tag{77}$$

Eq. 77 illustrates the strong dependence of the flux pattern on a small initial deflection in that $\sqrt{2}\,\theta$ is generally not small in comparison with C.

V. 6. Longitudinal Decay of Maximum Flux

The decay of the filament of maximum flux is defined by Eq. 69 and Eq. 70. Using the binominal expansion for the numerator and denominator of $G(\eta)$ it is easily shown that

$$\lim_{\eta \to 1} G(\eta) = 0.5 \tag{78}$$

and that

$$\lim_{\eta \to 0} G(\eta) = \exp(-0.5) = 0.6065 \tag{79}$$

In the region close to the jet nozzle η is approximately equal to 1 so that Eq. 69 becomes

$$\lim_{\eta \to 1} \frac{\overline{(u^2)}_m}{(u^2)_o} = \frac{D^2}{4C^2x^2} \tag{80}$$

Comparison with Eq. 42, shows that in this region the decay is identical with that for a deeply submerged jet.

As the filament of maximum flux approaches the free surface η tends to zero and Eq. 69 becomes

$$\underset{\eta \to 0}{\text{Lt}} \quad \frac{\overline{(u^2)}_m}{\overline{(u^2)}_0} = 0.303 \frac{D^2}{C^2 x^2} \tag{81}$$

Unless $\theta = 0$, this should only be expected to apply when $x = x_s$.

Fig. 11 shows that η remains approximately equal to 1 for a considerable distance downstream from the nozzle and then changes rapidly to zero. Thus a log-log plot of $[\overline{(u^2)}_m / \overline{(u^2)}_o]^{\frac{1}{2}}$ versus x/D may be expected to be linear, with a slope of -1 and an intercept, when x/D = 1, of 0.5/C for $\eta \triangleq 1$. It will then change rapidly to reach the limiting value given by Eq. 81 as η becomes equal to zero. For a jet with zero initial deflection the plot beyond this point would be defined by Eq. 81, and would again be linear, but with an intercept of 0.551/C.

Fig. 12 shows such a plot of the data from Ref. (9) for the $\frac{1}{2}$-in. jet with $x_o/D = 2$. Eq. 69 is plotted for C = 0.083 and $\theta = 3^o$. Also shown is the predicted behavior for $\theta = 0$.

V. 7. Determination of the Experimental Constants

The procedure used in Section IV. 1. could not be used in this case to determine C and x_o since Eq. 67 requires that η be less than 1. Due to experimental scatter in determining the location of the maximum experimental values slightly greater than 1 can occur.

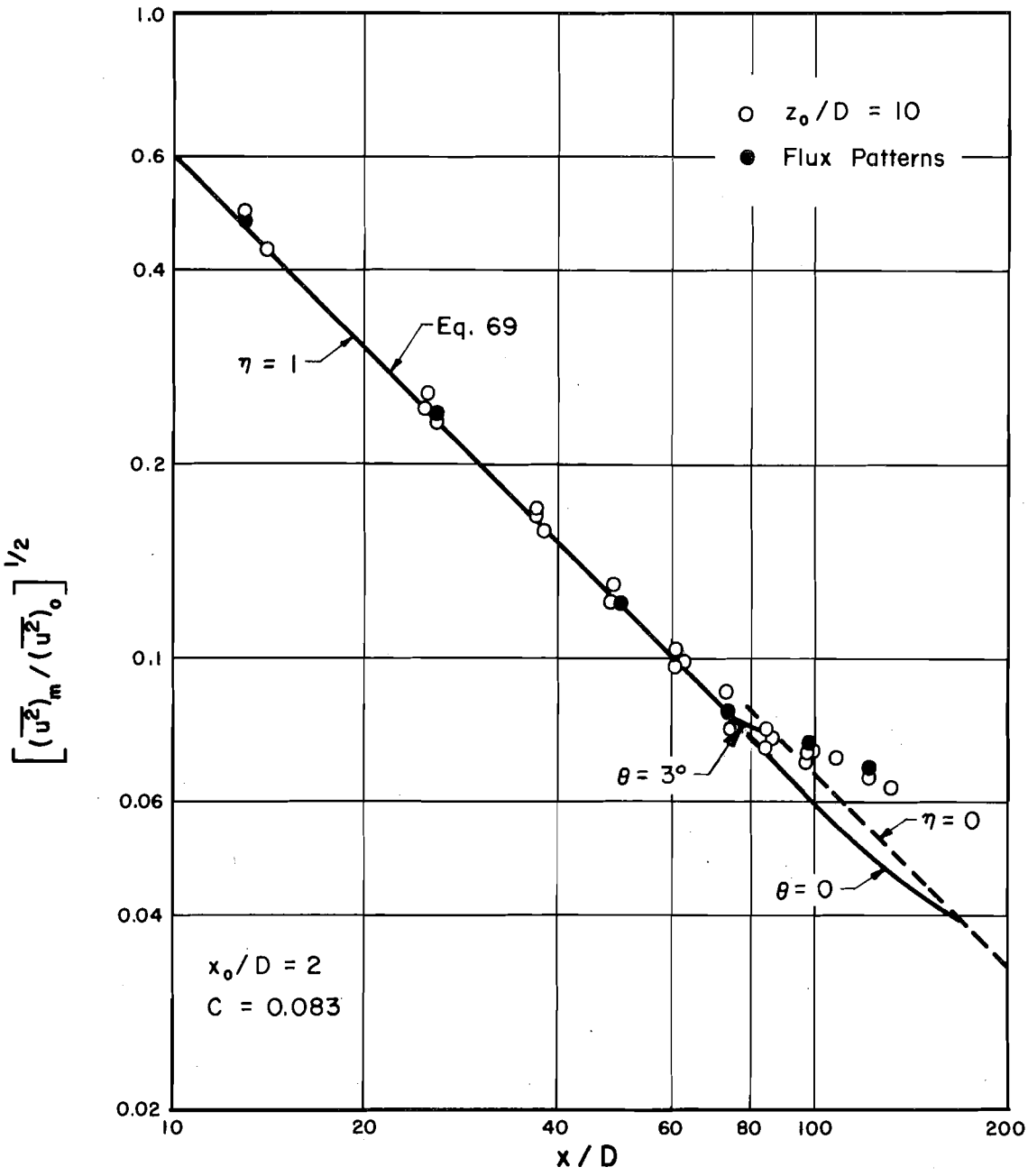

Fig. 12 — Longitudinal decay of maximum flux for shallow submerged jet with small initial upward deflection.

The procedure used was to prepare plots as shown in Fig. 10 and Fig. 12 and assume different values of C and x_o until those values were found which gave agreement between data and theory for both the lateral and longitudinal distributions. These values were C = 0.083 and x_o = 1 ins. θ was then determined from Fig. 11.

V. 8. Isoflux Patterns

Eq. 65 and Eq. 66 define the isoflux patterns. After some manipulation these give:

$$\left(\frac{s}{x}\right)^2 = C^2 \ln\left\{\frac{(\overline{u^2})_m}{\overline{u^2}} \frac{(1+\eta)^{\frac{\eta+2}{4}}}{(1-\eta)^{\frac{\eta-2}{4}}} \cosh\left[\frac{-2z(z_o-\theta x)}{C^2 x^2}\right]\right\} - \left(\frac{z}{x}\right)^2 \qquad (82)$$

Fig. 11 indicates, that, beyond doubt, the maximum flux has not reached the free surface for x/z_o = 7.4, i.e. when x_m = 3 ft. for the $\frac{1}{2}$-in. jet with an initial inclination of 3^o. Thus, Eq. 82 may be expected to apply. Fig. 13 shows a comparison between the isoflux line for $\overline{u^2}/(\overline{u^2})_m$ = 0.25 computed using Eq. 82 and the experimentally determined line taken from Fig. 6 of Ref. (9). There is good agreement except near the free surface where the data indicate a tendency to spread. It is easy to show by differentiation of Eq. 82 that the isoflux lines for all values $\overline{u^2}/(\overline{u^2})_m$ must cross the free surface (z = 0) normally. Thus, Eq. 82 will not indicate any tendency to spread. This may result from the fact that disturbances of the free surface have been ignored and that only the longitudinal velocity components have been included in the mathematical model.

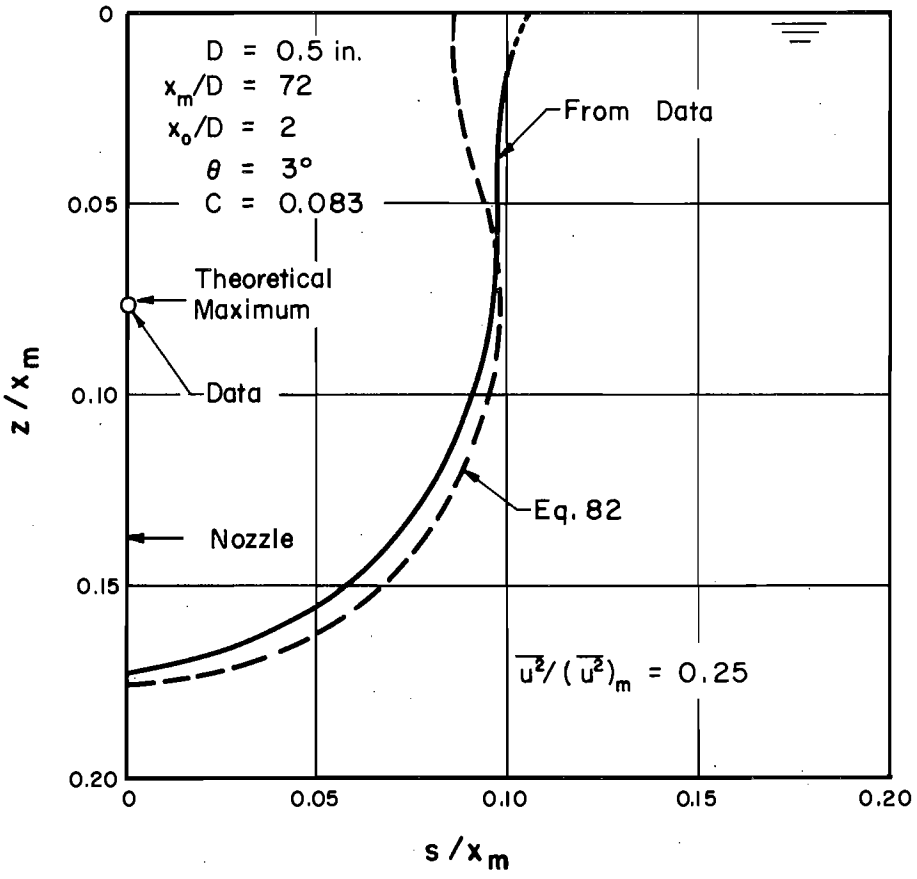

Fig. 13 — Isoflux line for shallow submerged jet with small initial upward deflection.

From Fig. 7 and Fig. 8 (9) this tendency to spread increased with increasing distance downstream. Further experimental data were collected to obtain further information on this tendency to spread. These are described in the next section.

V. 9. New Data on Spreading

Before collecting the data described below the instrument carriage described in Ref.(9)was redesigned and rebuilt using aluminum angle trusses in place of the wooden ladders used previously. The carriage rails were levelled by referencing a point gage mounted on the carriage to a still-water surface. The point gage could be read to 0.001 ft. With the new carriage and rail system deflections due to changes in humidity were no longer a problem and monitoring with the precision cathetometer as described in Ref. (9) was discontinued.

Some preliminary experiments were conducted to determine the minimum submergence at which a horizontal $\frac{1}{2}$-in. diameter jet would remain completely submerged at all times. This was found to occur for a submergence of 3 diameters. For lesser submergences the jet would be free part of the time. Even at the 3 diameter submergence a plume of spray was thrown into the air a short-distance downstream from the nozzle and fell back into the water. The surface was consequently quite disturbed and no attempt was made to collect any data closer than 2 ft from the nozzle.

The advantage of using such a shallow submergence is that the maximum flux reaches the free surface a short distance downstream from the nozzle. The tendency to spread may therefore be studied for greater distances downstream in the existing apparatus.

The original $\frac{1}{2}$-in. jet had been removed and a new installation was used for the experiments described in this section. At the time the experiments were conducted the authors were unaware of the large effect of a small deflection on the flow pattern. The bulk of the data were collected at 4 ft, 5 ft, and 6 ft downstream from the nozzle, except for one vertical centerline traverse and one horizontal traverse at z = 0.100 ft at a distance of 2 ft downstream from the nozzle. These latter two traverses are therefore the only data available to check on the initial deflection of the jet. Since the initial submergence of the jet is so small the effect of the image jet may be expected to have spread downward substantially at a distance of 2 ft downstream from the nozzle. Consequently the procedure outlined for the determination of the experimental constants in Section V. 7. may not be applied. The only apparent method available is to use a trial and error procedure to try to match the available distributions using Eq. 64.

This process of trial and error was in fact applied and the results are shown in Fig. 14. The best agreement was judged to occur for Cx = 0.150 ft and θ = 0.0025 radians. This choice matches the vertical data for the lower part of the jet and provides the correct distribution shape at z = 0.100 ft, and provides agreement with the vertical location of the maximum.

Choosing Cx = 0.138 ft and θ = 0.005 provides closer agreement with the maximum but leads to reduced agreement for the lower part of the vertical distribution and for the lateral distribution. Since it was noted for the data at five diameters submergence that there is a tendency for spreading at the free surface (i.e. measured values of flux are higher

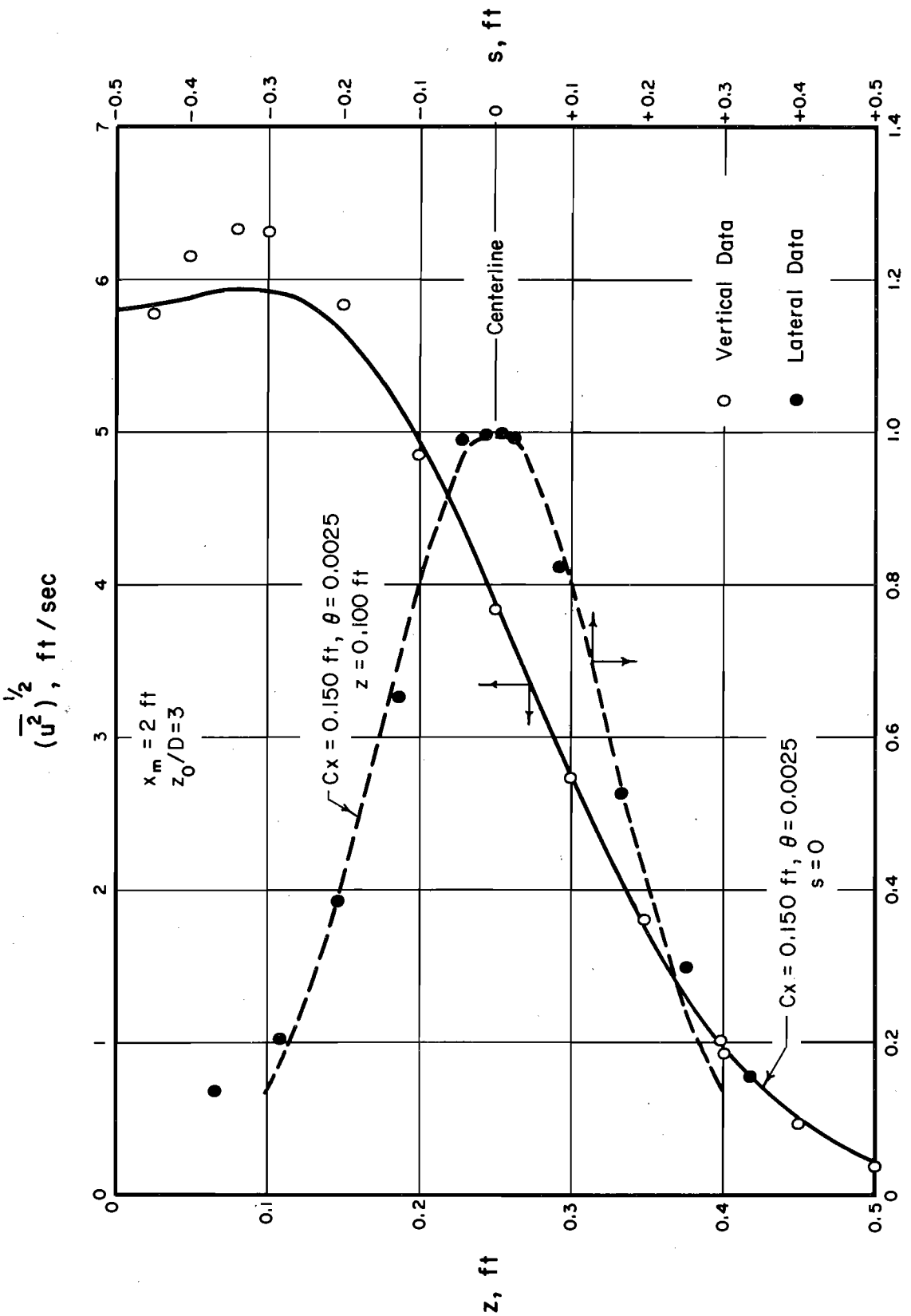

Fig. 14 — Vertical and horizontal flux profiles for jet submerged three diameters below free surface.

than the values expected from the mathematical model) the choice of C_x = 0.150 ft and θ = 0.0025 radians appears to be appropriate. Although this cannot be regarded as conclusive the analysis does indicate that the initial upward deflection of the jet was extremely small. It provides no means for determining x_o.

The data collected at distances of 4 ft, 5 ft, and 6 ft downstream from the nozzle are summarized in Figs. 15, 16, and 17. They show that the tendency to spread becomes more pronounced with distance downstream. One might speculate on the basis of these patterns that the flow pattern will ultimately approximate that for the lower half of a slot jet.

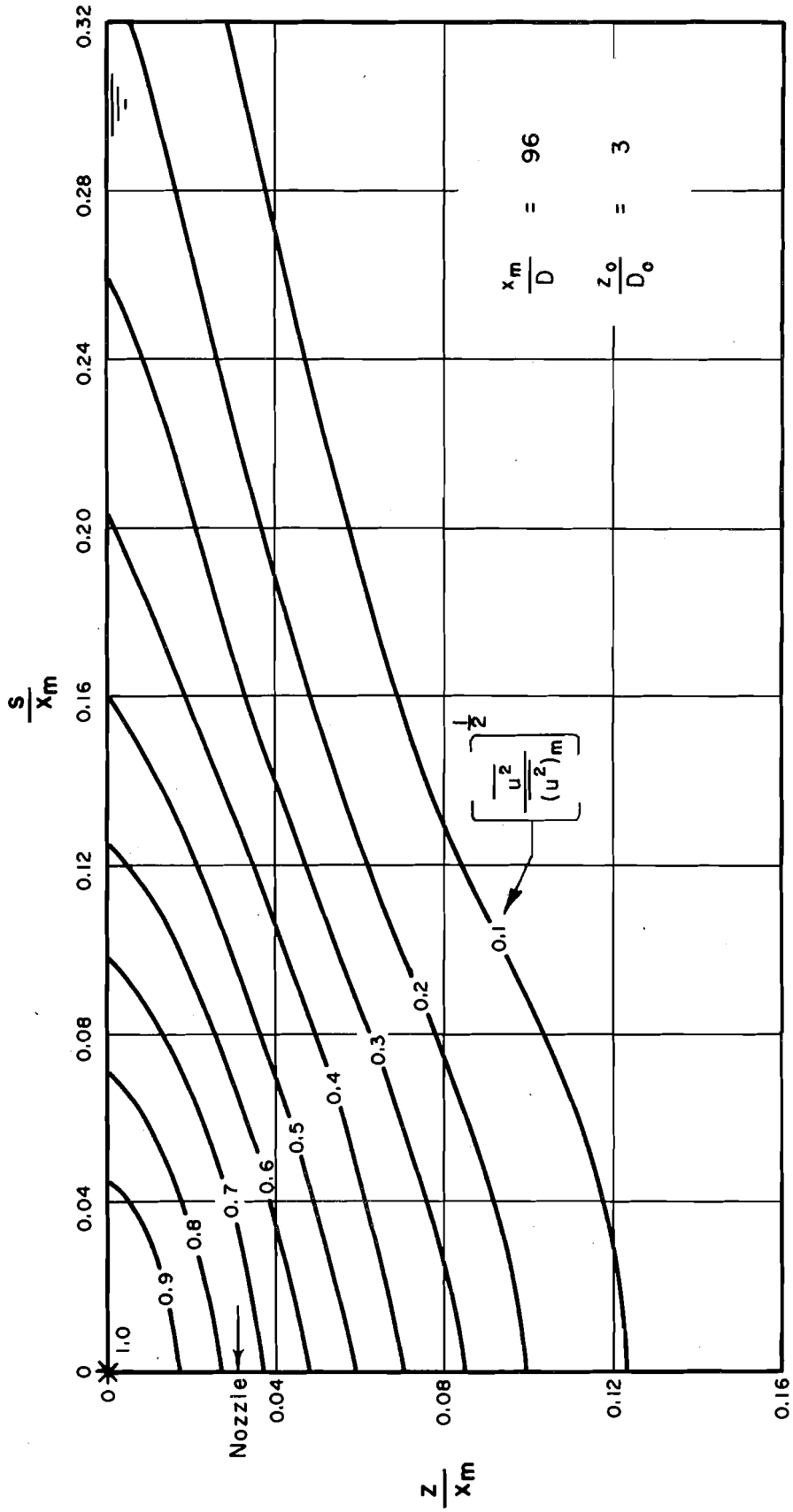

Fig. 15 — Isoflux patterns for shallow submerged jet. $x_m/D = 96$, $z_o/D = 3$, $D = \frac{1}{4}$ in.

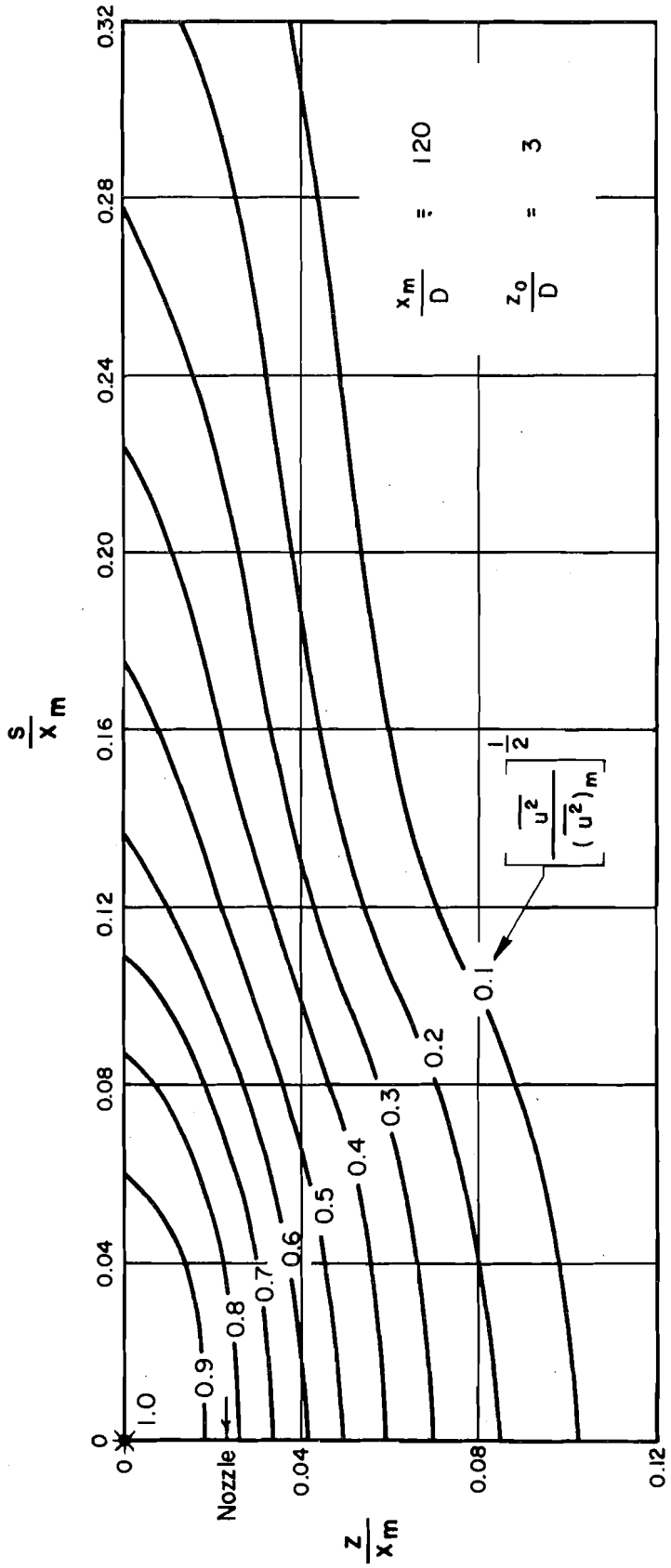

Fig. 16 — Isoflux patterns for shallow submerged jet. $x_m/D = 120$, $z_o/D = 3$, $D = \frac{1}{4}$ in.

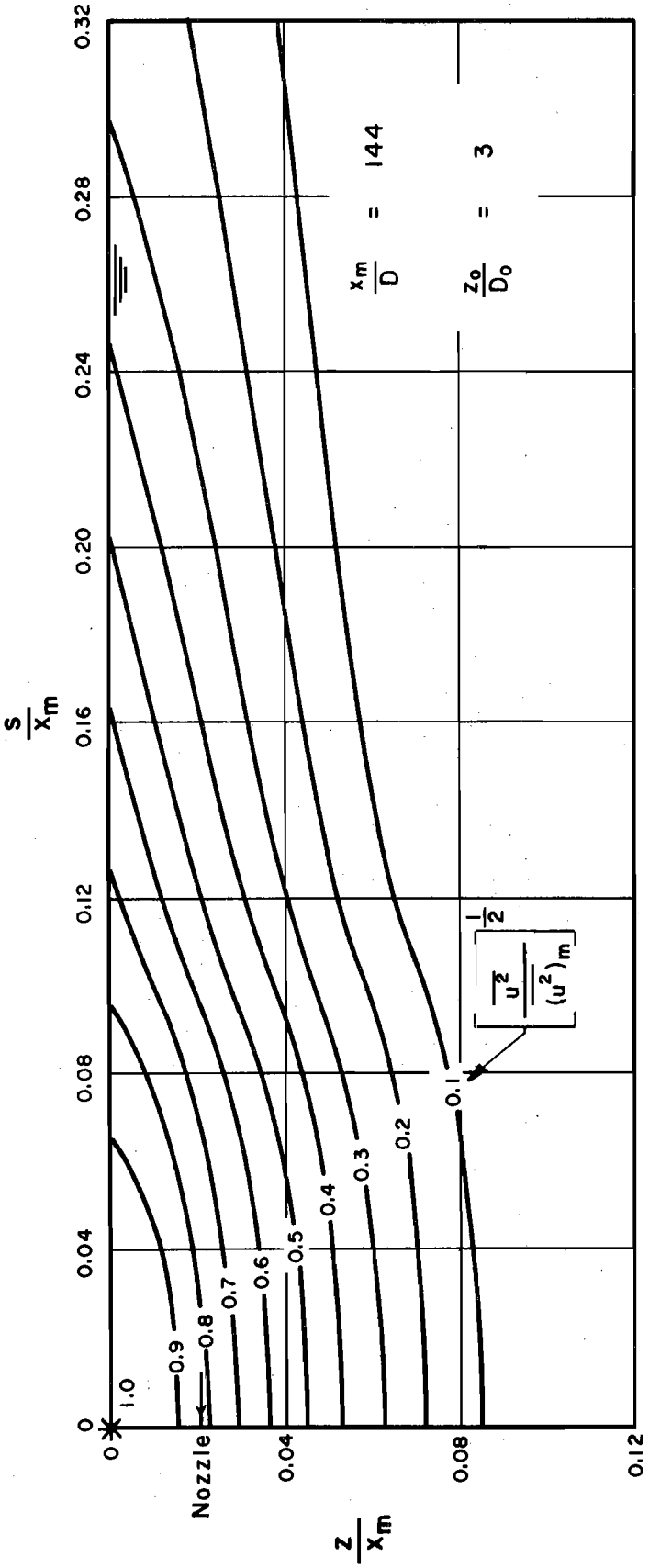

Fig. 17 — Isoflux patterns for shallow submerged jet. $x_m/D = 144$, $z_o/D = 3$, $D = \frac{1}{2}$ in.

VI. SHALLOW SUBMERGED JETS IN SHALLOW RESERVOIRS

VI. 1. Introduction

This chapter of the report is concerned primarily with the presentation of data collected for horizontal circular submerged jets emerging from a nozzle of $\frac{1}{2}$-in. diameter in close proximity to a free surface and a plane horizontal or gently downward sloping bottom. Insufficient time remained to permit a thorough analysis of the data and complete development of a mathematical model. Thus, all data are presented in terms of the measured longitudinal distance x_m and curves or lines drawn through the data points will be subject to slight shifts when the zero correction is later applied. A preliminary indication of a suitable mathematical model will be given.

VI. 2. Apparatus and Procedure

The experiments were conducted in the same apparatus, as used previously (9), except for the installation of an adjustable plane bottom. Care was taken to insure that the jets issued with zero initial upward deflection from the nozzle. The same procedure as before was used for the collection of the data except that a total head tube with an outside diameter of 0.083-in. and inside diameter of 0.0595-in. was substituted for the pitot tubes used previously, thus permitting a closer approach to the free surface and lower boundary. The total head reading was referenced to the reading from the side ports of a pitot tube located at a fixed vertical location about 4-in. to the side and 4-in. downstream of the

static tube and shielded inside a 1-in. diameter plexiglass tube with small holes drilled in its wall.

The plane lower boundary was constructed of two butting 1/8-in. thick stainless steel plates, one 12-ft by 4-ft, the other 12-ft by 3.25-ft. The joint was made rigid by fastening the edges of the plates to a 12-ft by 3-in., 3/16-in. thick steel lap plate on their lower side. Screw heads were countersunk to maintain a smooth upper surface. Screw heads were conical flat-topped and recessed in conical holes.

The plates were mounted on a supporting gridwork constructed of angle iron. The connections were again made with screw heads countersunk to maintain a smooth upper surface. Adjustment bolts were provided on the lower side to permit compensation for the initial deflection of the supporting framework.

A hinge assembly was provided at the upstream end of the plate support framework, with the hinge center-line coincident with the 12-ft long upstream edge of the plate, so that rotation of the plate did not produce any change in the vertical location of the plate edge. The back edge of the plate butted against the vertical wall through which the nozzle issued. The entire assembly was supported on two rows of three jacks each, one row at the upstream end and one at the downstream end. The downstream jacks were adjustable and permitted tilting of the plate from the horizontal to slopes of up to 20%. Data was collected for slopes of 0, 5%, and 10%, the slope being defined as the sine of the downward angular deflection of the plate.

With the plate set in the horizontal position (but not submerged) adjustments were made so that the elevation at any location did not deviate from that for a true plane by more than $\pm$ $\frac{1}{2}$-mm on the scale of a precision

cathetometer with a 10-second bubble located just outside the reservoir on the side and at about the location of the plate center-line. After this initial trueing of the plate, slopes were set using a cathetometer with a 40 second bubble and scale divisions of 1 mm located at the downstream end of the apparatus just outside the reservoir in line with the nozzle.

VI. 3. The Effect of the Lower Boundary

Previous experiments by Cowley (4) on a plane vertical boundary indicated that the jet moved toward the boundary in a similar manner to that observed for jets close to a free surface. Consequently one would expect that when a jet is close to both a free surface and a plane lower boundary that the "attraction" of the two boundaries will be in competition and that the behavior of the jet will ultimately be determined by the boundary which exerts the greater influence. Different behavior is to be expected for different submergences and different elevations above the lower boundary since these variables will largely determine which boundary will play the dominant role. The experiments were designed with this likelihood in mind and the observed behavior is discussed in later sections.

VI. 4. Form of Mathematical Model

The mathematical model will be much more complex than for the case of the free surface only having an influence on the flow pattern. The flow is now complicated by the existence of a shear stress along the wall so that momentum flux is no longer conserved.

It is expected that a hybrid solution of the form proposed by Glauert (5) for the wall jet may be suitable. In other words a solution for the region remote from the wall will be matched with a solution for the region close to the wall. It is proposed to investigate a solution similar to that in Chapter V for the region remote from the wall except that an image jet will be placed equidistant below the wall to represent the cutoff of lateral momentum flux by the wall. The complete solution of such a model requires, however, that the influence of the images of the images in the free surface and bed be considered. The solution therefore is represented by an infinite series which is not apparently readily simplified or manipulated. A simplified model which ignores the images of the images gives, for a horizontal bed:

$$\frac{\overline{u^2}}{(\overline{u^2})_o} = \frac{D^2}{4c^2x^2}\left\{\exp\left[-\frac{s^2+(z-z_o)^2}{c^2x^2}\right]+\exp\left[-\frac{s^2+(z+z_o)^2}{c^2x^2}\right]+\exp\left[-\frac{s^2+(z-z_o-2z_1)^2}{c^2x^2}\right]\right\} \qquad (83)$$

in which z_1 = the vertical distance from the center-line of the nozzle to the plane bed. The origin of the co-ordinates x, s, and z is in the free surface.

When s = 0, differentiation of Eq. 83 should yield the vertical location of the filament of maximum flux for some distance downstream of the nozzle until the growing boundary layer along the wall exerts a marked influence.

The model given by Eq. 83 includes the tendency of the filament of maximum flux to move toward either the free surface or the bed, depending on which exerts the dominant influence.

VI. 5. Experimental Program

The experiments which were conducted included the measurement of vertical and lateral flux distributions, location of the filament of maximum flux and measurement of the decay of maximum flux with distance from the nozzle for several combinations of z_o/D, z_1/D and bed slope S. Since many natural basins and reservoirs have bed slopes lying between 0 and 10% the slopes investigated were 0, 5%, and 10%. For some combinations isoflux patterns were obtained. All tests were conducted using a $\frac{1}{2}$-in. diameter horizontal nozzle with an efflux velocity of 40.6 ft/sec. The effluent and receiving water were at the same temperature and density. The results of the experiments are discussed in the following sections.

VI. 6. Gaussian Distribution of the Lateral Flux Profiles

Eq. 83 may be written:

$$\frac{\overline{u^2}}{(\overline{u^2})_o} = \frac{D^2}{4C^2x^2} \exp\left[-\left(\frac{s}{Cx}\right)^2\right] \left\{ \exp\left[-\left(\frac{z-z_o}{Cx}\right)^2\right] + \exp\left[-\left(\frac{z+z_o}{Cx}\right)^2\right] + \exp\left[-\left(\frac{z-z_o-2z_1}{Cx}\right)^2\right] \right\} \tag{84}$$

For any fixed values of z_0, z_1, and z the peak flux at any x will occur for y = 0 and is given by:

$$\frac{(\overline{u^2})_p}{(\overline{u^2})_o} = \frac{D^2}{4C^2x^2} \left\{ \exp\left[-\left(\frac{z-z_o}{Cx}\right)^2\right] + \exp\left[-\left(\frac{z+z_o}{Cx}\right)^2\right] + \exp\left[-\left(\frac{z-z_o-2z_1}{Cx}\right)^2\right] \right\} \tag{85}$$

Combining Eq. 84 and Eq. 85 then gives

$$\frac{\overline{u^2}}{(\overline{u^2})_p} = \exp\left[-\left(\frac{s}{Cx}\right)^2\right] \tag{86}$$

The flux distribution given by Eq. 86 depends on x. This dependence may be removed, however, by letting $s = s_{\frac{1}{2}}$ when $[\overline{u^2}/(\overline{u^2})_p]^{\frac{1}{2}} = 0.5$ so that

$$(Cx)^2 = \frac{s_{\frac{1}{2}}^2}{\ln 4} \tag{87}$$

Combining Eq. 86 and Eq. 87 then yields

$$\left[\frac{\overline{u^2}}{(\overline{u^2})_p}\right]^{\frac{1}{2}} = 2^{-\left(\frac{s}{s_{\frac{1}{2}}}\right)^2} \tag{88}$$

It may be noted that Eq. 86 and Eq. 88 would not be altered if all the images were included in the mathematical model.

Fig. 18 shows a comparison of the averaged data at different values of z, for the conditions indicated, with Eq. 88. The method of obtaining the averages is illustrated in Fig. 19. The data were plotted as shown and an average curve was drawn. Points on the average curve were then transferred to Fig. 18. It may be noted that Fig. 19 includes data quite close to the bed at $x_m/D = 144$. Data close to the free surface did not agree with Eq. 88 and is not included.

Although Eq. 88 was developed from a simplified mathematical model for the case of a horizontal bed it shows good agreement with the data for bed slopes of 0, 5, and 10%. This illustrates the existence of Gaussian lateral flux distributions under a variety of experimental conditions.

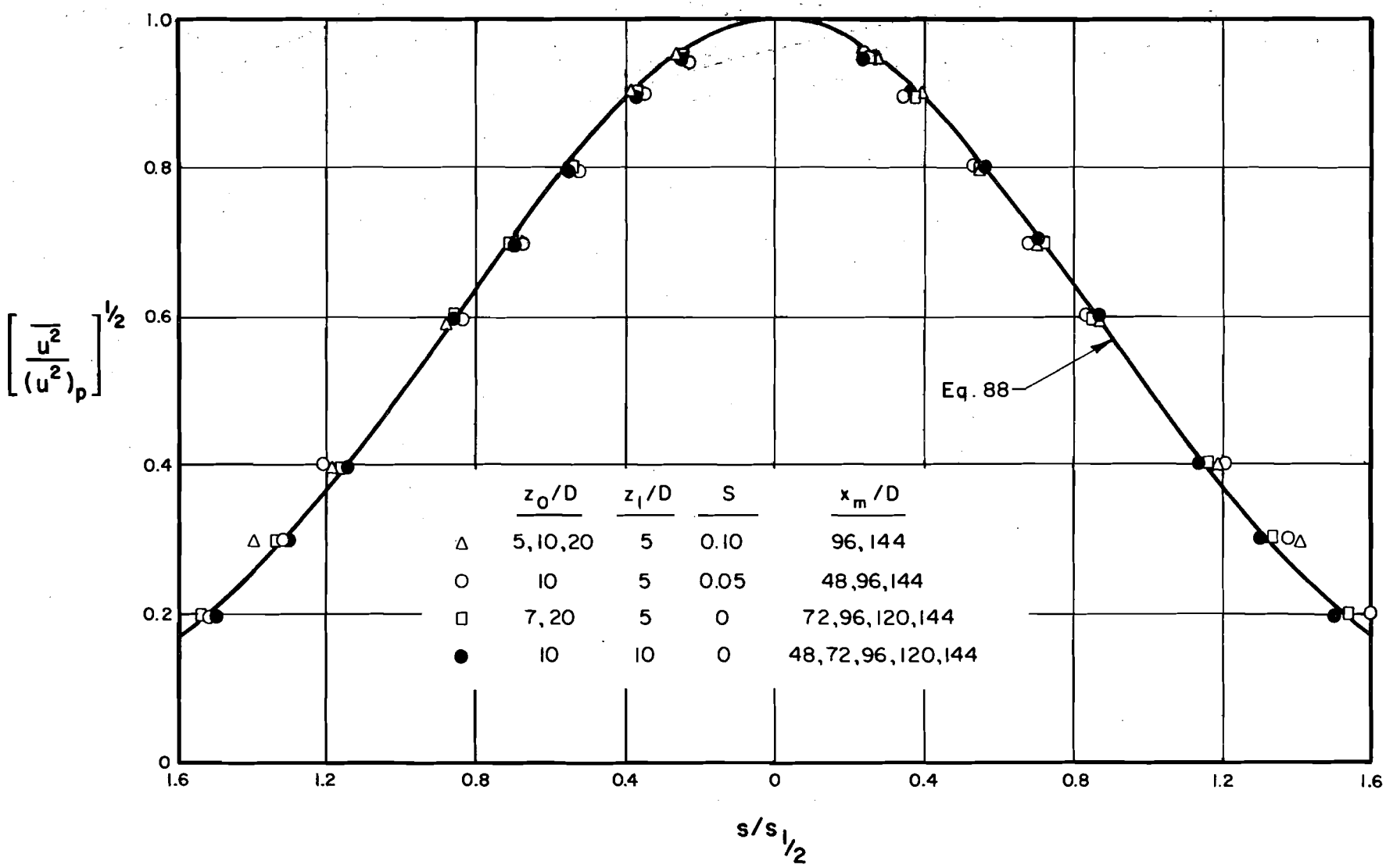

Fig. 18 — Gaussian distribution of horizontal flux profiles for shallow submerged jets in shallow reservoirs.

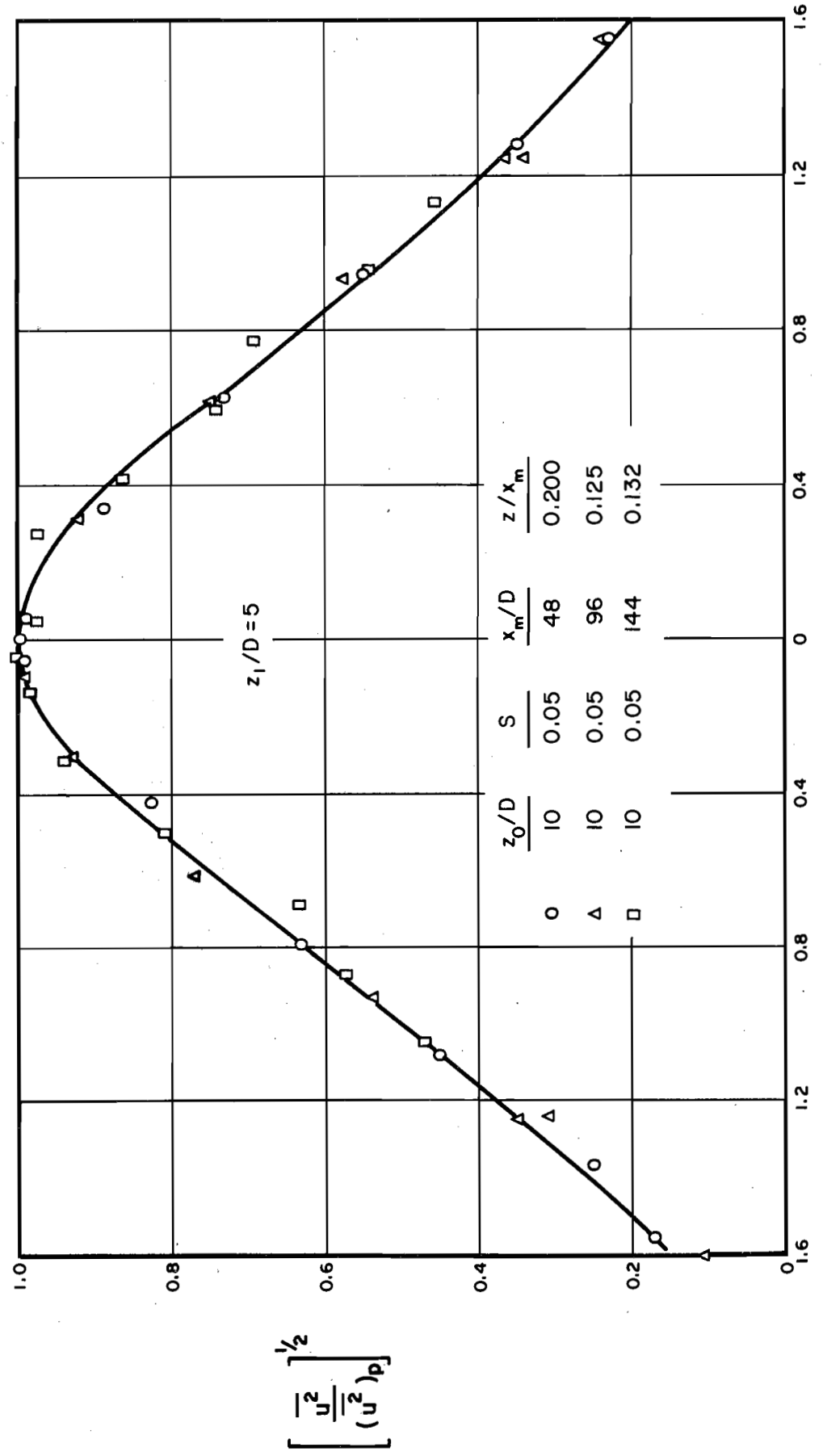

Fig. 19 — Distribution of horizontal flux profiles for shallow submerged jet in shallow reservoir.

VI. 7. Location of the Filament of Maximum flux

Fig. 20 shows a plot of the location of the filament of maximum flux when the bed slope was zero and the nozzle was located 5 diameters above the bed. When the free surface was 5 diameters above the nozzle two maxima were found to occur beyond 50 diameters from the nozzle. One moved toward the free surface and the other toward the bed. For all higher submergences of the nozzle the influence of the bed was dominant and the maximum moved toward the bed.

The upper part of Fig. 21 shows the behavior at different nozzle submergences for $z_1/D = 5$ and $S = 0.05$. For both 5 and 7 diameters submergence the influence of the free surface was dominant, whereas the influence of the bed was dominant for submergences of 10 diameters and higher.

The lower part of Fig. 21 shows the behavior at different nozzle submergences for $z_1/D = 5$ and $S = 0.10$. At 5 diameters submergence of the nozzle the maximum again moves to the free surface. For 10 and 20 diameters submergence however, either the bed and the free surface have insufficient influence to cause the maximum to deviate from the nozzle center-line elevation or their effects nullify each other.

VI. 8. Longitudinal Decay of Maximum Flux

Figs. 22 and 23 illustrate the decay of the maximum flux for the conditions shown in Figs. 20 and 21. The data are found to deviate from the straight line representing the behavior of a deeply submerged jet beyond the point at which the maximum starts to move toward either the bed

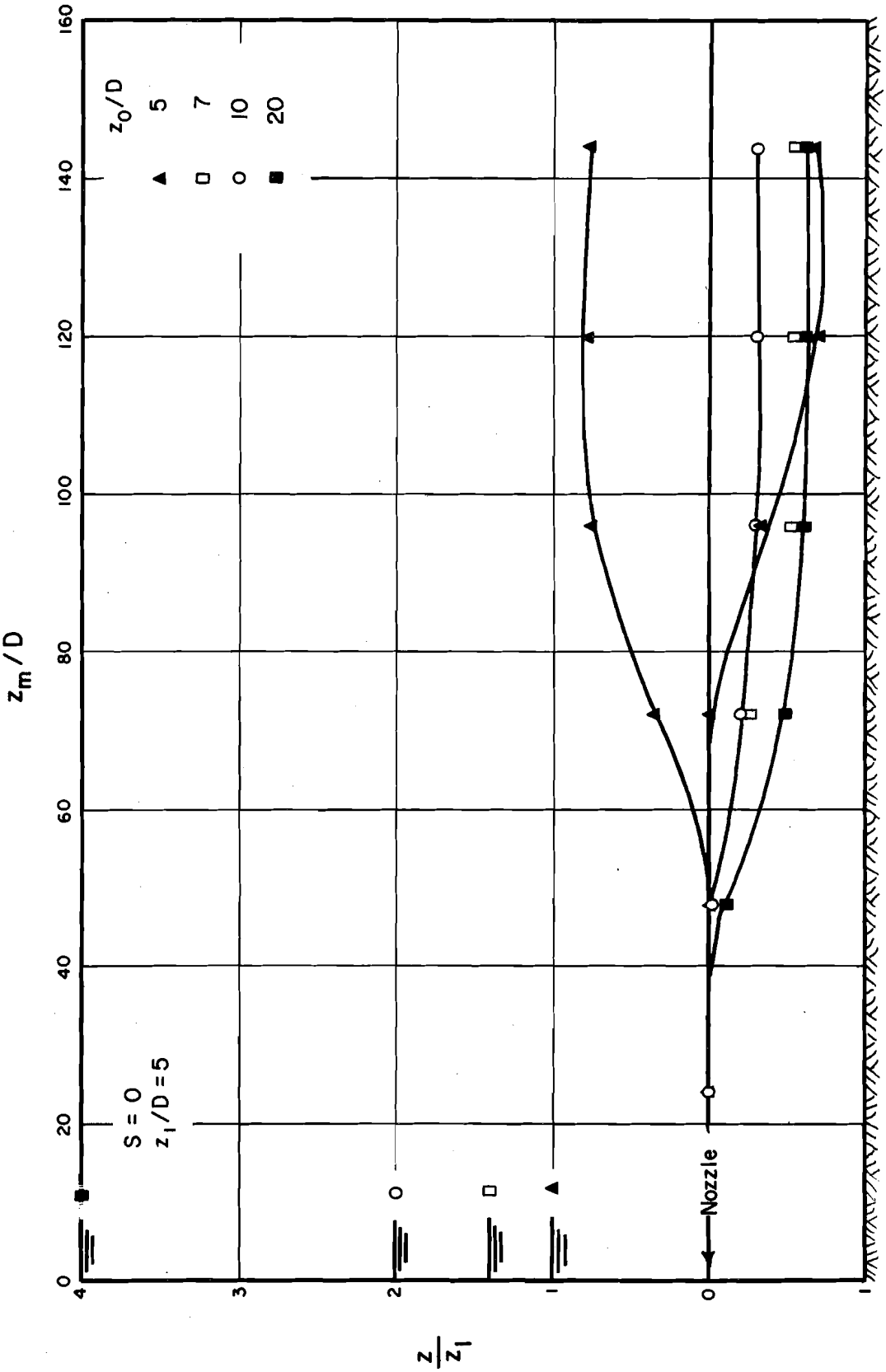

Fig. 20 — Vertical centerline location of maximum flux for shallow submerged jets in shallow reservoirs, S = 0.

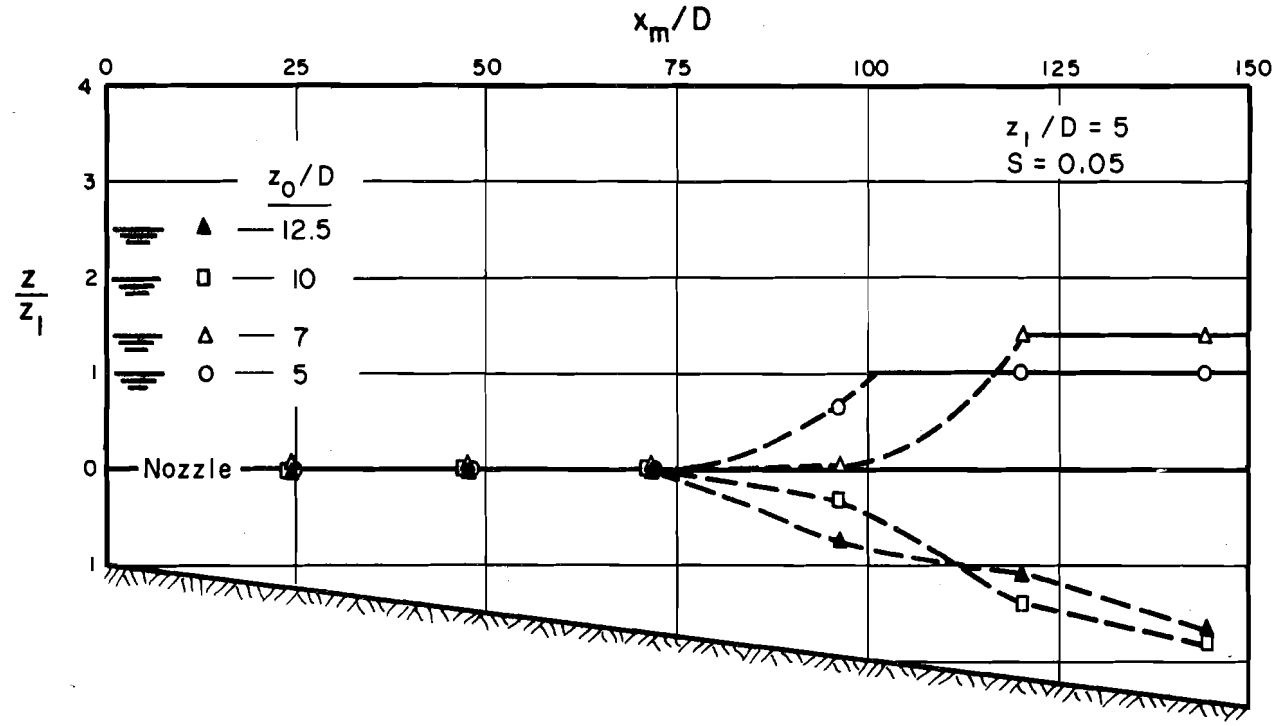

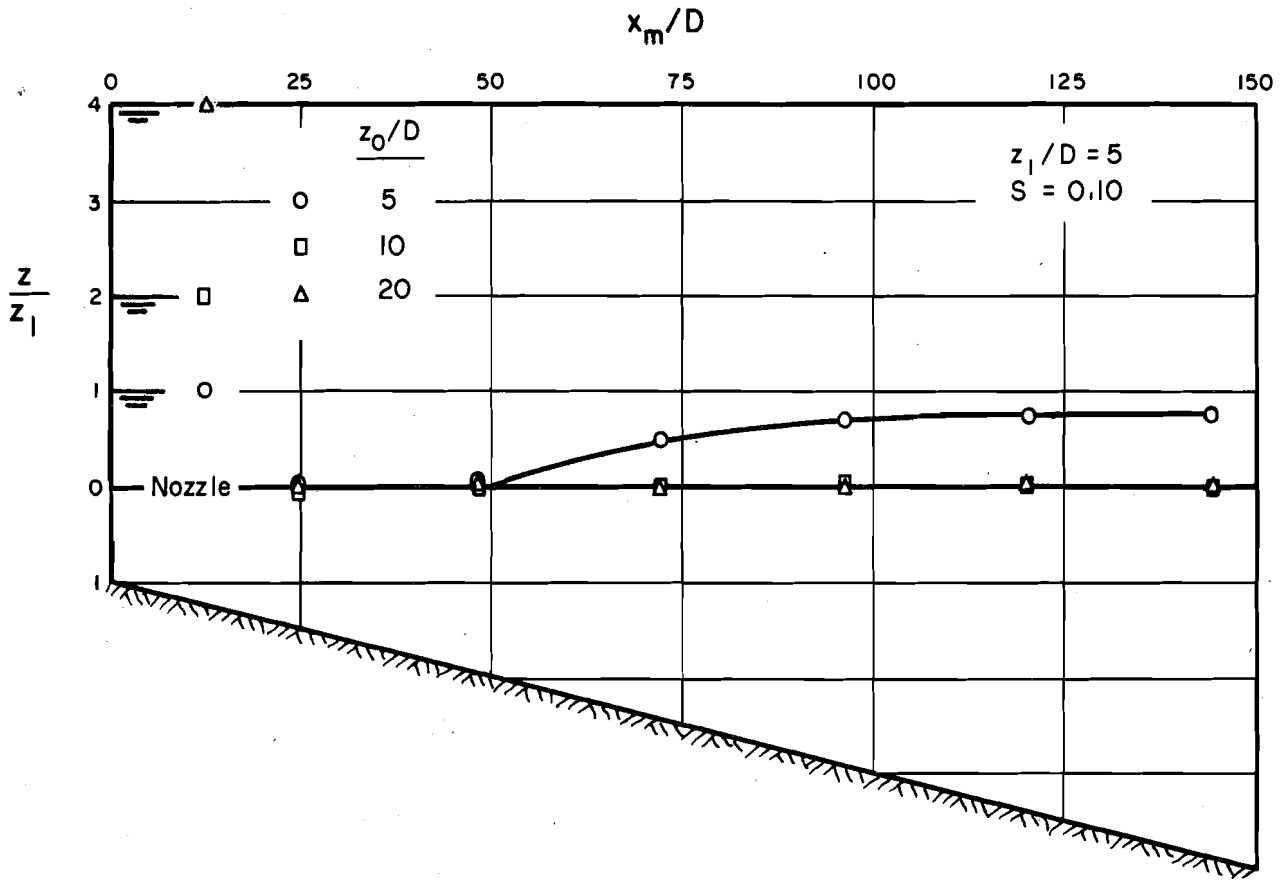

Fig. 21 — Vertical centerline location of maximum flux for shallow submerged jets in shallow reservoirs, S = 0.05 and S = 0.10.

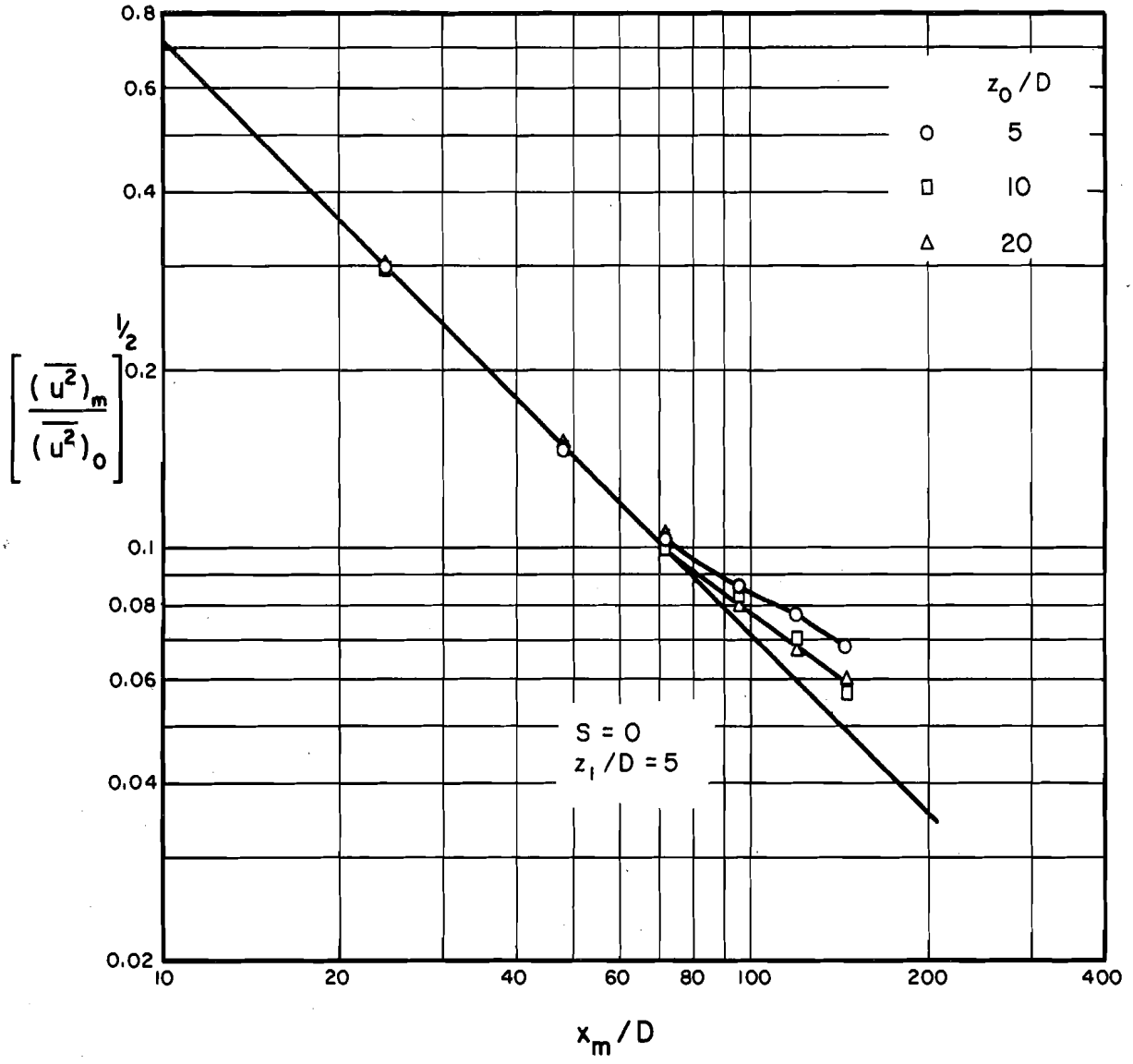

Fig. 22 — Longitudinal decay of maximum flux for shallow submerged jets in shallow reservoirs, S = 0.

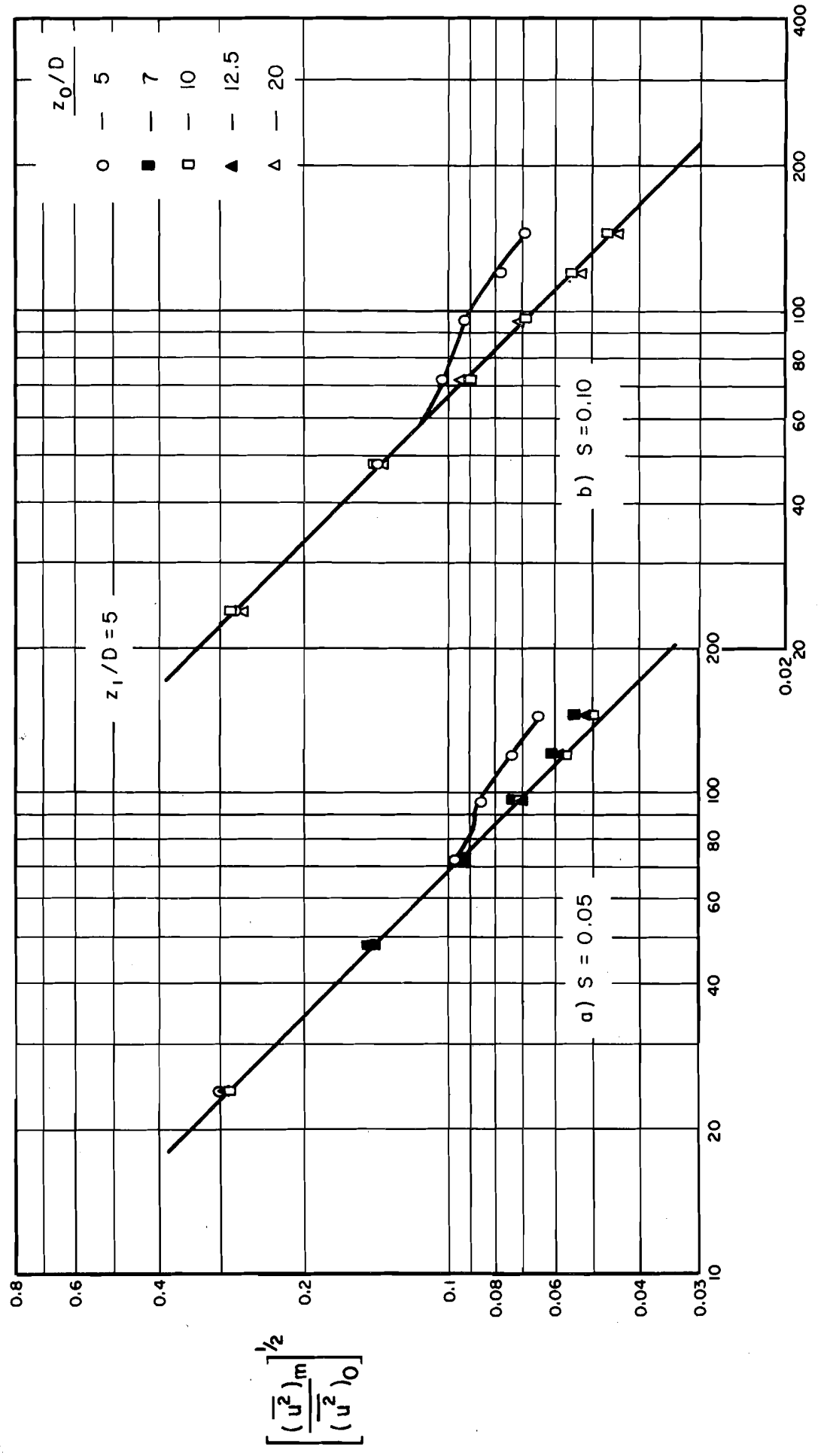

Fig. 23 — Longitudinal decay of maximum flux for shallow submerged jets in shallow reservoirs, S = 0.05 and S = 0.10.

or the free surface. It should be noted that the data are plotted in terms of the measured x and the zero correction is not included. This could have an influence in determining the value of the spread coefficient C. Preliminary indications are, however, that C is independent of the test conditions and is approximately equal to 0.08.

VI. 9. Isoflux Patterns

The isoflux patterns for $z_o/D = 10$, $z_1/D = 5$ and $S = 0$ are illustrated in Figs. 24 and 25 at distances of 48, 96, and 144 diameters downstream from the nozzle. The corresponding patterns for a bed slope of 5% are shown in Figs. 26, 27, and 28. The reader may, if he wishes, treat $\overline{u'^2}$ as negligible and regard these as isovel patterns.

These patterns were obtained by measuring vertical flux profiles at intervals on both sides of the center-line. Readings were taken to within $\frac{1}{4}$-in. of the free surface and the bed.

No attempt has been made on these figures to define the variation of the flux pattern in the region very close to the bed where the gradients must be steep to satisfy the condition that the velocity at the bed be zero.

It may be noted that the bed exerts a much stronger influence on the flow pattern when the slope is zero as would be expected. For both slopes, however the pattern bears little resemblence to that for a deeply submerged jet and there is a marked tendency for the flow to spread out across the wall as well as at the free surface.

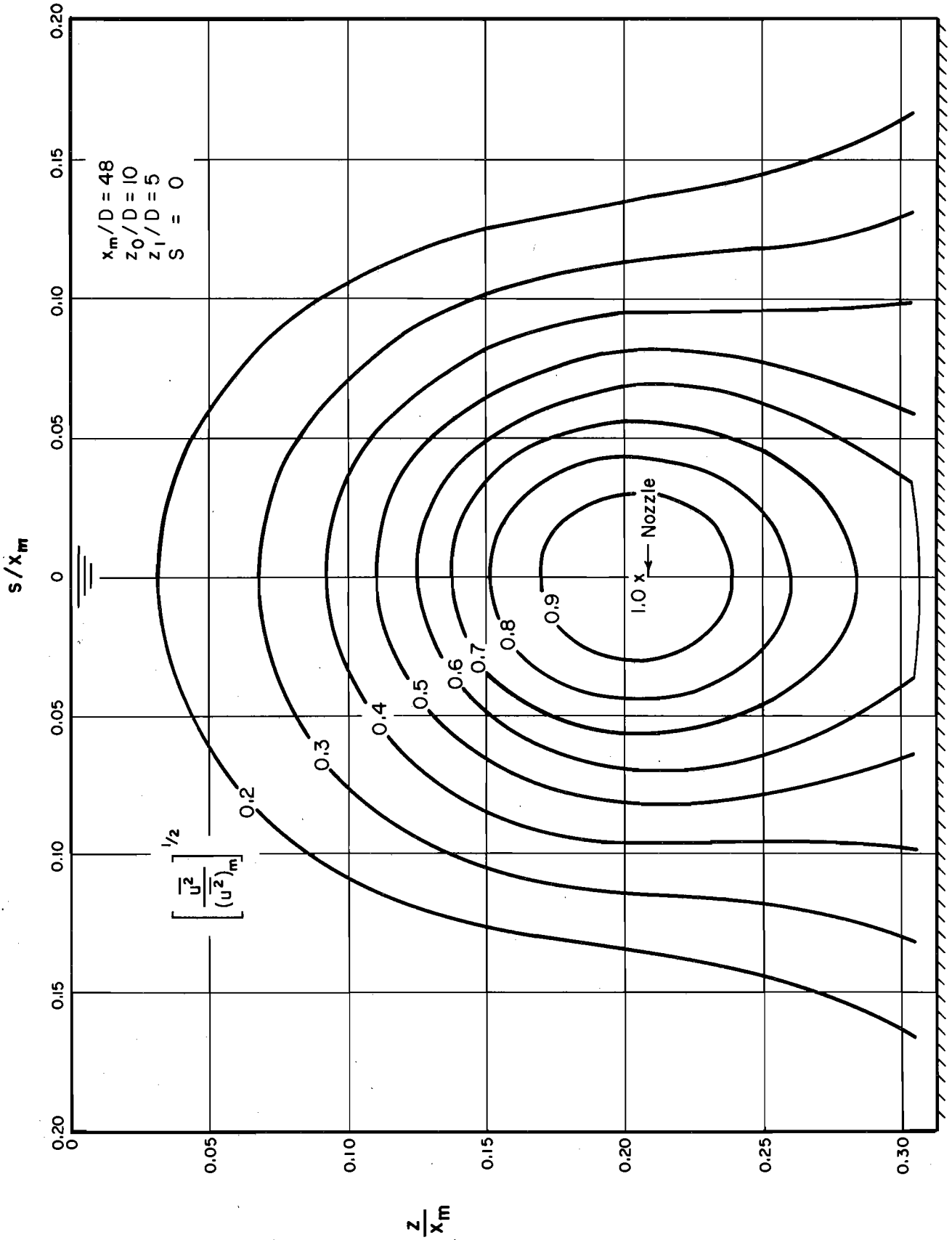

Fig. 24 — Isoflux pattern for shallow submerged jet in shallow reservoir, S = 0, $x_m/D = 48$, D = ½ in.

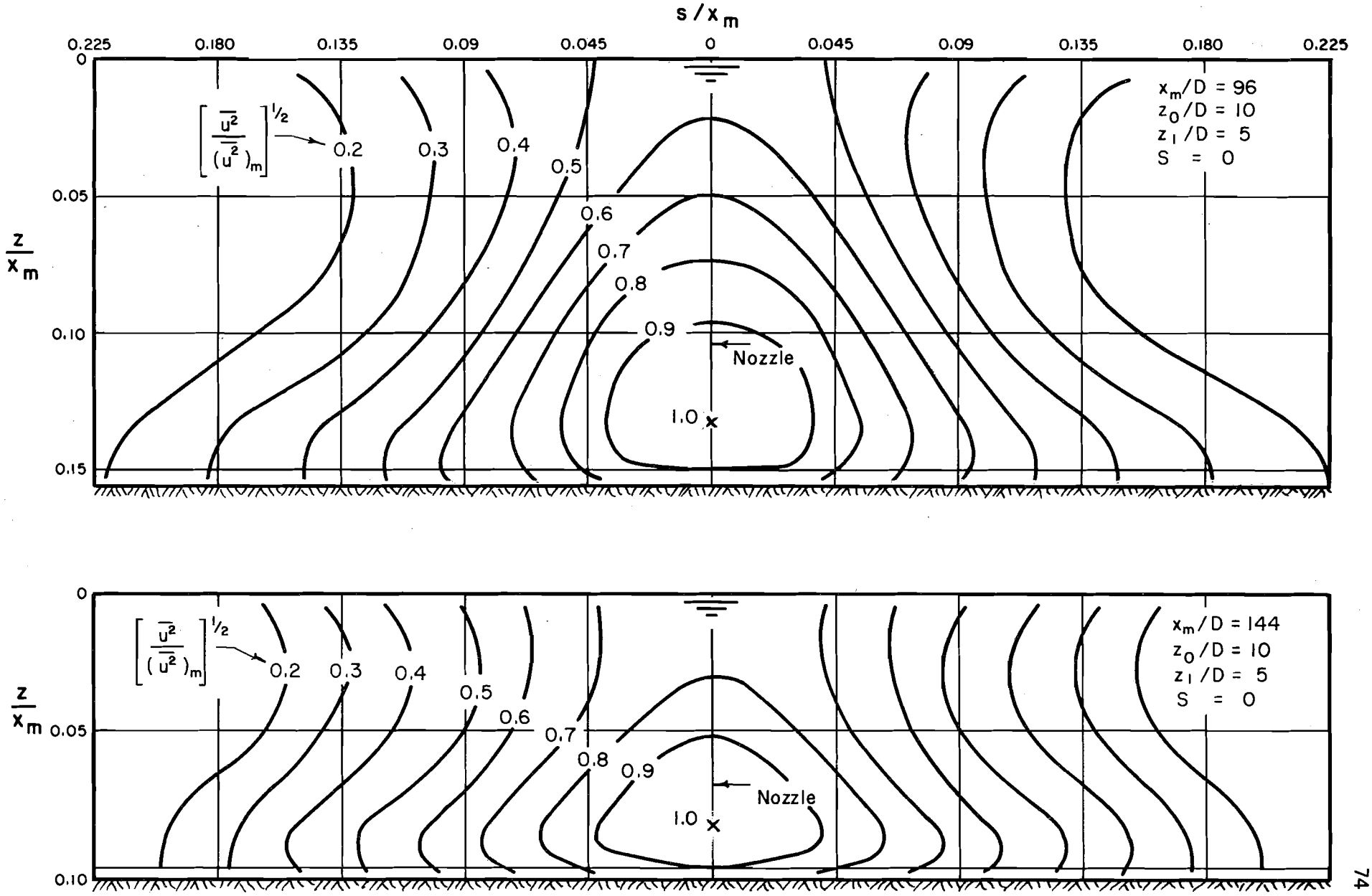

Fig. 25 — Isoflux patterns for shallow submerged jet in shallow reservoir, S = 0, x_m/D = 96 and 144, D = ½-in.

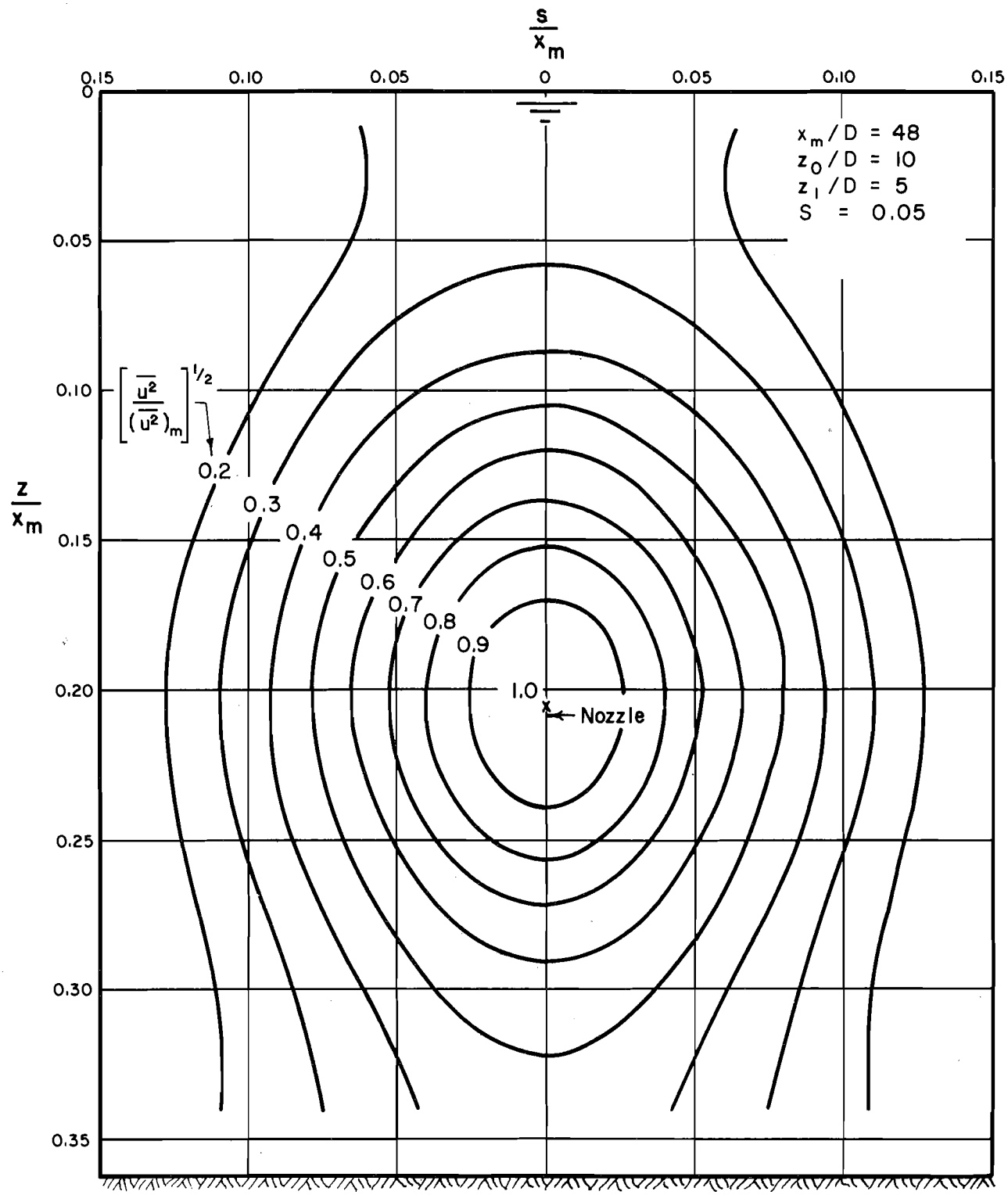

Fig. 26 — Isoflux pattern for shallow submerged jet in shallow reservoir, S = 0.05, x_m/D = 48, D = ½-in.

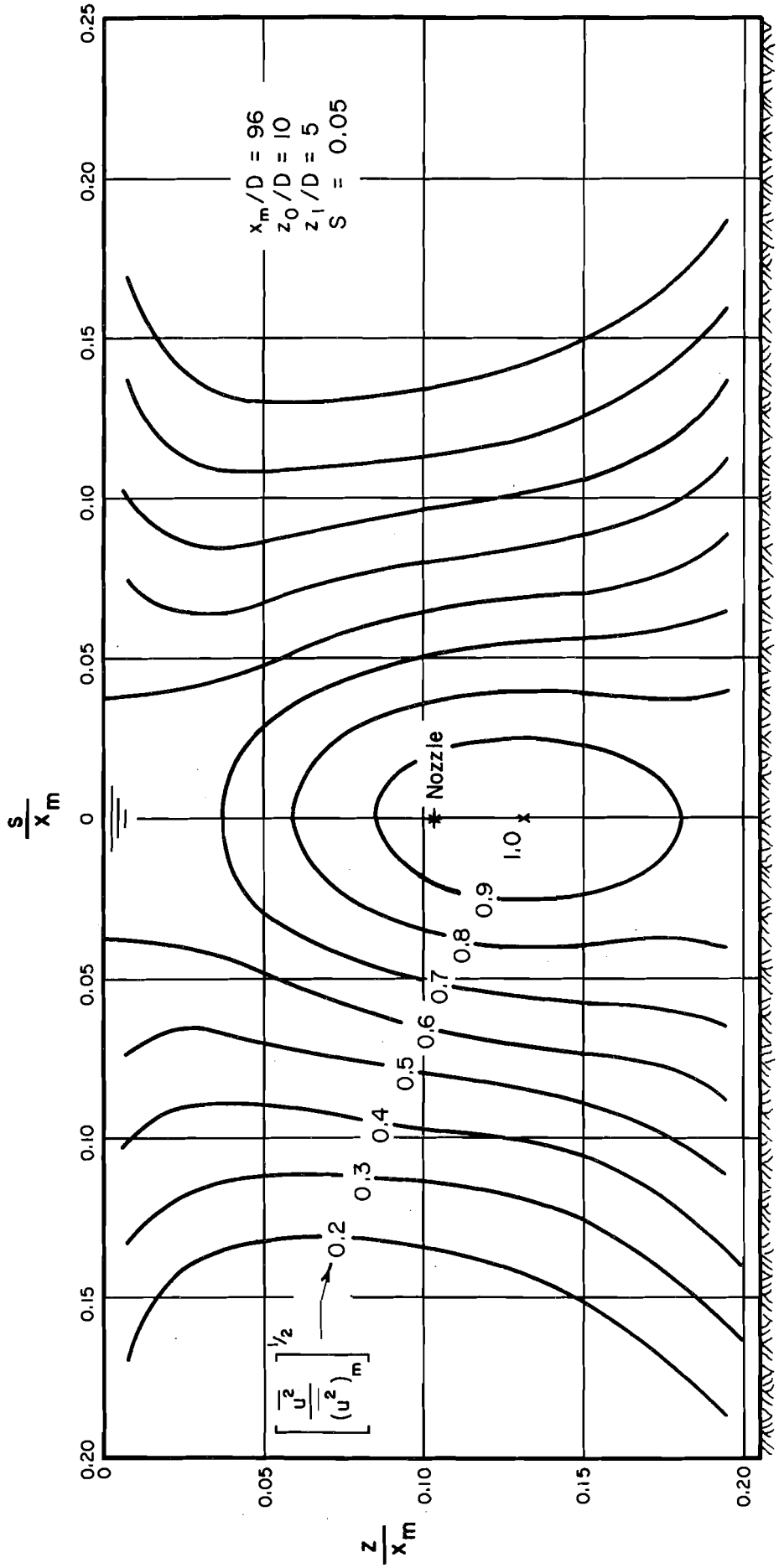

Fig. 27 — Isoflux pattern for shallow submerged jet in shallow reservoir, S = 0.05, $x_m/D = 96$, D = $\frac{1}{2}$ in.

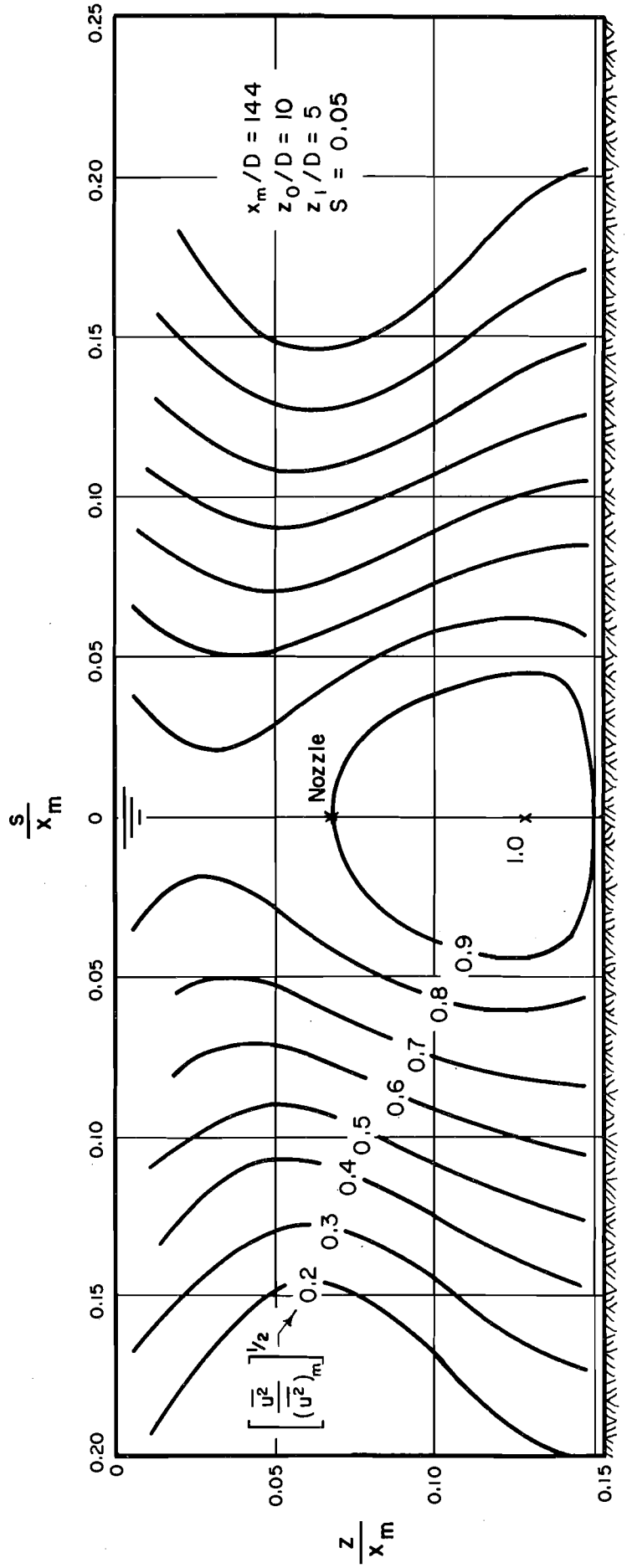

Fig. 28 — Isoflux pattern for shallow submerged jet in shallow reservoir, S = 0.05, $x_m/D = 144$, D = $\frac{1}{2}$-in.

VI. 10. Summary and Conclusions

The combined effect of a nearby lower boundary and free surface on a horizontal flow from a circular jet nozzle has been investigated experimentally with some preliminary analysis using a simplified mathematical model based on Reichardt's hypothesis.

The horizontal flux patterns have been shown to be Gaussian except in a zone of intense spreading near the free surface and very close to the lower boundary. The vertical location of the filament of maximum flux has been shown to depend on the relative influence of the upper and lower boundaries, both of which "attract" the maximum. The flux patterns have been found to be radically different from those of a deeply submerged jet far from any lower boundary and exhibit a strong tendency to spread over the lower boundary and at the free surface.

VII. CONCLUSIONS AND APPLICATIONS

VII. 1. Summary and Conclusions

Following an introductory review of theories for the analysis of the deeply submerged jet, Reichardt's hypothesis and Alexander, Baron, and Coming's generalization thereof have been considered to determine their usefulness in the analysis of jet flows with complex boundary conditions.

Solutions are obtained for flux distributions close to an axisymmetric submerged turbulent jet outlet. All solutions use tabulated probability functions or exponential functions. A comparison is made with momentum flux data for an axisymmetric flow and agreement is shown to be good at 1, 2, 4, 6, 8, and 10 diameters downstream from the outlet.

The generalized Reichardt hypothesis is employed to obtain Gaussian distributions for the flux of mass, heat, and momentum and permits superposition of elementary solutions. The analysis is presented for plane- and axi-symmetric flows. An adjustment to the origin of the data matches axial flux data with the mathematical model and defines a spreading coefficient, leading to a complete definition of the flux distribution.

The solutions are in the form of a distorted chi-square distribution, and two distorted normal distributions. Moreover, a simple solution beyond the potential core uses the axial distribution of flux to obtain the radial distribution directly. The analysis shows promise of providing straightforward solutions for free turbulent flows involving complex boundary conditions.

A simplified model, employing an image jet, is then developed to represent the momentum flux distribution for a jet with a small initial angle of inclination from the horizontal close to a free surface. This qualitatively predicts the observed behavior of such a jet for some distance downstream from the nozzle, until the maximum flux reaches the free surface. The quantitative agreement for the vertical location of the maximum flux at any longitudinal location downstream from the nozzle and for the decay of the maximum flux with longitudinal distance is found to be reasonably good within this range. Isoflux patterns agree reasonably well, except near the free surface where the simplified mathematical model fails to predict the observed intense lateral spreading. New experiments conducted at large distances downstream from a shallow submerged axisymmetric nozzle show that the tendency to spread laterally becomes more pronounced with increasing distance from the nozzle. The isoflux patterns appear to be tending toward those of the lower half a plane-symmetric flow.

Further experiments were conducted after the introduction of a plane-bed. Data were collected for a variety of jet submergences and positions of the bed. Several bed slopes were tested. Those indicated that the flux patterns were strongly influenced by the bed as well as the free surface. The vertical location of the maximum flux was found to depend on the relative influence or proximity of the bed and free surface to the jet nozzle. Both had an "attractive" influence on the jet. The flux patterns exhibit a strong tendency to spread at both the bed and the free surface.

There was insufficient time to permit a rigorous and complete development of a suitable Reichardt model. However, a simplified model, using image jets to represent the bed and free surface is suggested for the region of flow beyond the boundary layer at the bed. It is proposed that this be employed as the upper half of a hybrid solution. The suggested model qualitatively predicts the "attraction" of the bed and the free surface for the jet.

The use of Reichardt's hypothesis and its generalization therefore appear to have excellent potential for the study of complex jet flow patterns.

VII. 2. Application to Water Resources Problems

The experimental information presented herein provides some previously unavailable information on the behavior of shallow submerged jets. The influence of the free surface is found to cause behavior which has previously been observed for shallow submerged heated jets, the effects for these having been assumed to result solely from the density difference between the jet and the reservoir. It would appear, therefore, that a reevaluation of the role of density difference for such flows should be made. The tendency for the maximum flux to migrate toward a lower boundary also indicates that care must be taken in the location of submerged outfalls to insure that this characteristic will not result in undesirable scour.

The theoretical development using Reichardt's hypothesis and Alexander, Baron & Coming's generalization thereof indicates that these

provide a useful means for synthesising mathematical models which may be used to predict many features of complex jet flows qualitatively and some features quantitatively. The methods permit the prediction of the distributions of momentum flux, mass flux and heat flux. If the longitudinal turbulent fluctuations of velocity are ignored the momentum flux distributions reduce immediately to velocity distributions. The methods are immediately applicable in the design of submerged outfalls, syphon spillway outlets, lock discharge ports, in a prediction of the diffusion of tracers in streams, and in the simulation of streams discharging into reservoirs or the ocean. In order to develop a suitable mathematical model, the flow pattern is assumed to consist of a distribution of infinitesimal point or line source jets, together with image jets to represent the boundaries. The fact that linear superposition is possible greatly simplifies the application.

LIST OF REFERENCES

1. Albertson, M. L. et al., "Diffusion of Submerged Jets," Trans. Amer. Soc. Civ. Engrs., Vol. 115, 1950, pp. 639-697.

2. Alexander, L. G., Baron, T., and Comings, E. W., "Transportation of Momentum, Mass and Heat in Turbulent Jets," University of Illinois Bulletin, No. 413, May 1953.

3. Corrsin, S., "Investigations of Flow in Axially Symmetrical Heated Jet of Air," NACA Wartime Reports, ACR 3L23, 1943.

4. Cowley, J. E., "The Effect of a Plane Boundary on the Dispersion of a Submerged Jet," M.Sc. thesis, Dept. of Civil Eng., Queen's University, Kingston, Ont., 1962.

5. Glauert, M. B., "The Wall Jet," Jl. of Fluid Mechs., Vol. 1, Pt. 6, 1956, pp. 625-643.

6. Hinze, J. O., "Measurement of Mean Values of Static Pressure and Velocity," Turbulence, McGraw-Hill Book Co., New York, 1959, pp. 132-137.

7. Hinze, J. O., "Measurement of Turbulence Quantities in a Round Free Jet," Turbulence, McGraw-Hill Book Co., New York, 1959, pp. 431-439.

8. Hinze, J. O., "Mixing Length and Phenomenological Theories," Turbulence, McGraw-Hill Book Co., New York, 1959, pp. 277-293.

9. Maxwell, W.H.C., and Pazwash, H., "Basic Study of Jet Flow Patterns Related to Stream and Reservoir Behavior," Univ. of Illinois Water Res. Center Research Rpt. No. 10, July, 1967, 63 pp.

10. Pearson, E. S., and Hartley, H. O., eds., Biometrica Tables for Statisticians, Vol. 1, Cambridge University Press, Cambridge, England, 1954, pp. 122-129.

11. Reichardt, H., "On a New Theory of Free Turbulence," Zamm, Vol. 21, No. 5, Oct., 1941 and translation by Flint, M., Jl. Roy. Aero. Soc., Vol. 47, 1943, pp. 167-176.

12. Schlichting, H., "Cylindrical Co-ordinates," Boundary Layer Theory, McGraw-Hill Book Co., New York, 1955, pp. 49-50.

13. Schlichting, H., "Mean Motion and Fluctuations," Boundary Layer Theory, McGraw-Hill Book Co., New York, 1955, pp. 370-371.

14. Schlichting, H., "Derivation of the Stress Tensor of Apparent Turbulent Friction from the Navier-Stokes Equations," Boundary Layer Theory, McGraw-Hill Book Co., New York, 1955, pp. 373-376.

15. Schlichting, H., "Theoretical Assumptions for the Calculation of Turbulent Flows," Boundary Layer Theory, McGraw-Hill Book Co., New York, 1955 pp. 383-399.

16. Schlichting, H., "Free Turbulent Flows; Jets and Wakes," Boundary Layer Theory, McGraw-Hill Book Co., New York, 1955, pp. 483-506.

17. Tollmein, W., "Calculation of Turbulent Expansion Processes," Zamm, Vol. 6, 1926, pp. 468-478 or NACA Technical Memorandum, TM1085, 1945.

18. Zelen, M., and Severo, N. C., "Probability Functions," Handbook of Mathematical Functions, Abramowitz, M., and Stegun, I. S., eds., National Bureau of Standards, Applied Mathematics Series No. 55, Washington, D.C., March 1965, pp. 925-995.

19. Folsum, R. G., "Review of the Pitot Tube," Trans. ASME, Oct., 1956, pp. 1447-1460.

20. Prandtl, L., and Tietjens, O. G., "Velocity Measurement with Pitot-static Tube," Applied Hydro- and Aeromechanics, Dover Publications, New York, 1957, pp. 229-231.